Inversion of PP Seismic Wavefield and PS Converted Wavefield Arrival Times for the Estimation of a Model of Subsurface P and S Velocities: A Level Set Approach

Carlos Andrés Niño Niño

Dissertation for the degree of Doctorate in Engineering.

Thesis advisor

Daniel Sierra Bueno, Ph.D.

Co-advisor	Co-advisor
Cesar Duarte Gualdron, Ph.D.	William Mauricio Agudelo, Ph.D.

Universidad Industrial de Santander

Facultad de Ingenierías Fisicomecánicas

Escuela de Ingenierías Eléctrica, Electrónica y de Telecomunicaciones

Doctorado en Ingeniería, Área Ingeniería Electrónica

Bucaramanga

2024

Dedication

To the process that leads us to believe we understand, to comprehend that we actually don't understand, and to start anew until we once again believe we understand.

To my family: Pablito, Conchita, Gustavo, Monica and Juan Esteban.

To the great moments I lived by your side MM, although now I must think that they did not exist.

Acknowledgements

I thank Professor Cesar Duarte for allowing me to learn with him. To Engineer William Agudelo for his knowledge and his time to help me understand it. To Professor Daniel Sierra for his guidance.

To the time given to me by Ivan Sanchez of great value. To **Hugo Torres**, Jairo Bautista, Daniel Meneses and Jheyston Serrano for being there in the most difficult moments.

This work was developed in the framework of Colombian Ministry of Science and Technology Doctoral Grant 647. The authors thank Ecopetrol S.A and CEMOS and GISEL research groups belonging to the School of Electrical and Electronic Engineering of Universidad Industrial de Santander for allowing time for the development of the methodology PS tomography and numerical implementation. The BivLab and HDSP research groups, belonging to the School of Systems Engineering at the Universidad Industrial de Santander, are acknowledged for allowing the use of their computing infrastructure to execute the developed algorithm.

Table of content

List of figures

List of Tables

List of appendixes

Glossary

1. **Adjoint operators Method:** The adjoint-state is a general method to compute the gradient of a functional that depends on a set of state variables, which are solutions of forward equations. The adjoint variables are the solutions of an linear system and can be seen as variables which gather a global measure of the perturbation of the problem with respect to the state variables. Numerically this approach is attractive because only one extra linear system needs to be solved and often the computation of the gradient with respect to the model parameters is equivalent to one or two evaluations of the forward modelling. This cost is often almost independent of the number of model parameters, which is not always the case when the Fréchet derivatives are computed. However the adjoint-state method does not provide the sensitivity of the solution to errors. For that, the Fréchet derivatives are needed or a Monte Carlo type of methods with a large number of forward computations are required, (Plessix, 2006).

2. **Fast sweeping:** It is an iterative method that uses upwind differencing for discretization and applies Gauss-Seidel iterations with alternating sweeping ordering to solve the discretized system. The idea is that each sweeping ordering follows a family of characteristics of the corresponding Eikonal equation in a certain direction simultaneously, (Zhao, 2005).

3. **Fast marching methodology:** The key feature of the algorithm is a carefully selected order of traveltime evaluation. At each step of the algorithm, every grid point is marked as either Alive (already computed), NarrowBand (at the wavefront, pending evaluation), or FarAway (not touched yet). Initially, the source points are marked as Alive, and the traveltime at these points is set to zero. A continuous band of points around the source are marked as NarrowBand, and their traveltime values are computed analytically. All other points in the grid are marked as FarAway and have an “infinitely large” traveltime value. An elementary step of the algorithm consists of the following moves: among all the narrowBand points, extract the point with the minimum traveltime, mark this point as alive, check all the immediate neighbors of the minimum point and update them if necessary, (Fomel, 1997).

4. **Geological Reflector:** An interface between layers of contrasting acoustic, optical or electromagnetic properties. Waves of electromagnetism, heat, light and sound can be reflected at such an interface. In seismic data, a reflector might represent a change in lithology, a fault or an unconformity, (Yilmaz, 2001).

5. **Illumination**:Seismic wave energy falling on a reflector and thus available to be reflected. It depends on source-receiver configuration and velocity distribution, especially irregular velocity contrasts that bend raypaths differently than adjacent raypaths, and the target dipping angle. Important aspect in areas with complex velocity variations, such as around high-velocity contrasts or beneath salt deposits, (Bording et al., 1987).

In complex structures, it is possible that wave energy penetrate only weakly into some areas, or not at all causing seismic shadows (i.e., the illumination problem). Deficiencies in seismic illumination can be mitigated if deep subsurface sources are used in acquisition, (Bording et al., 1987).

6. **Inverse problems:** Inverse theory is an organized set of mathematical techniques for reducing data to obtain knowledge about the physical world on the basis of inferences drawn from observations. The observations of the world will consist of a tabulation of measurements, or data. Questions to be solved to answer will be stated in terms of the numerical values (and statistics) of specific (but not necessarily directly measurable) properties of the world. These properties will be called model parameters. The term inverse theory is used in contrast to forward theory, which is defined as the process of predicting the results of measurements (predicting data) on the basis of some general principle or model and a set of specific conditions relevant to the problem at hand. Inverse theory, roughly speaking, addresses the reverse problem: starting with data and a general principle, theory, or quantitative model, it determines estimates of the model parameters. Inverse problems of mathematical physics may be broadly described as problems of determining the internal structure or past state of a system from indirect measurements. Many inverse problems can be modeled abstractly as $Kx = g$, where K is a given operator between appropriate function spaces, g is given by measured "external" parameters, and the desired solution x represents "internal" parameters,

which are inaccessible to direct measurement. In the important special case when K is a compact linear operator, it is well known that the problem of determining x is generally ill-posed in the sense of Hadamard, and it is this ill-posedness that engenders peculiar problems in the numerical approximation and interpretation of solutions, (Engl and Groetsch, 2014).

7. **Ill-posed problems:** That either has no solutions within the desired class, or has many (at least two) solutions, or the solution procedure is unstable (small errors in the measurement data may lead to indefinitely large errors in the solutions). Most difficulties in solving ill-posed problems are caused by instability. Therefore, the term "ill-posed problems" is often used for unstable problems, (Kabanikhin, 2008).

8. **Level set:** The general idea is to apply a function $\phi((x,z),t)$ to the space the interface inhabits, where $p = (x,z)$ is a point in that space, t a point in time. The function is initialized at $t = 0$, and then a scheme is used to approximate the value of $\phi((x,z),t)$ over small time increments. To initialize $\phi((x,z),t)$ at each point of the mesh means that $\phi((x,z),t) = \pm d$, where d is the distance from point p to the curve at time $t = 0$. The $\pm$ sign of the distance d indicates whether the point is inside or outside a region: it is negative if it is inside and positive if it is outside. The positive sign is used if the point p is outside the closed curve; the negative sign is used if the point p is inside the closed curve (Osher and Fedkiw, 2005).

   At any time t_0, the evolving curve corresponds to the locus of all points p such that

$\phi((x,z),t) = 0$, and that locus is a level curve of the ϕ function. The locus of all points (x,z) such that $\phi((x,z),t) = c$, contour around the original curve, where c is an arbitrary positive or negative constant. A computationally intensive algorithm is used to set up the initial value of function ϕ at each of the mesh points. For each mesh point, the distance between it and each point on the curve is determined and the minimum value is set as the mesh point's ϕ value. Clearly, as the curve evolves in time, the value of the function ϕ at each mesh point evolves too (Osher and Fedkiw, 2005).

9. **Lagrange multipliers as adjoints:** Overall, Lagrange multipliers associated with a set of constraints can be viewed as "adjoints" that capture the sensitivity of the objective function to changes in those constraints. This perspective is particularly useful in optimization problems involving multiple constraints, where the Lagrange multipliers can be used to measure the relative importance of each constraint and guide the optimization process towards a feasible solution (Demanet, 2016).

10. **PS converted wave:** In seismic exploration, P-waves (also known as compressive waves) penetrate down into the earth. When a P-wave hits an interface (e.g., liquid-solid (as at the seafloor), or solid-solid (within the subsurface), the boundary conditions (continuity of stress and displacement) in general require the energy be partitioned, into both upgoing (reflected) and downgoing (transmitted) waves (both P and S). This occurs at every interface; the strength of conversion is included among the Knott-

Zoeppritz equations (of course there is no reflected shear wave at the seafloor). And similar conversions occur with incident S-waves (in anisotropic media, there are two shear modes in each direction which complicates the analysis). In exploration seismics, normally the most important of these various converted modes is the P-S conversion upon reflection; this is called the C-wave. As opposed to analysis of P-wave to P-wave (P-P) reflection, C-wave (P-S) analysis is more complex. C-wave analysis requires at least three times as many measurement channels per station. Variations in reflection depths can cause significant analytic problems, (Yilmaz, 2015).

11. **Residual:** In seismology, the traveltime residual is the difference between the observed travel time and a reference travel time predicted by a velocity model (Bording et al., 1987).

12. **Seismic method:** Involve the measurement of wave-fields produced by artificially-generated seismic waves that propagate in the subsurface or near the soil surface. Typically, seismic measuring arrays involve a transect of seismic sensors (geophones) deployed on the soil surface or along boreholes, and a seismic source is successively activated at different spatial locations. The geophones measure the ground movement resulting from body, including pressure (P) and shear (S) waves propagating through the soil, scattering at soil interfaces and from surface waves propagating at the soil surface. Pressure waves, produce soil displacement parallel to the direction of propagation and are the smallest in amplitude. Relative to pressure waves, shear waves

and surface waves are slower (both travelling at a similar velocity) but produce higher amplitude soil displacement that is perpendicular to the direction of propagation. Seismic velocities depend on properties of the bulk soil such as resistance to compression and to shear stress, but also on soil moisture and capillary pressure. For this reason, they provide a direct link to soil mechanical properties (e.g., penetration resistance), (Yilmaz, 2015).

13. **Seismic Tomography:** Seismic tomography is an imaging technique that uses seismic waves generated by earthquakes or explosions to create two and three dimensional images of Earth's interior. Seismic tomography is one of the main techniques to constrain the distribution of physical properties that affect seismic-wave propagation: elastic, anelastic, and anisotropic parameters, and density. Tomographic models often play a critical role in the analysis of the subsurface – lithology, temperature, fracturing, fluid content, etc. The term tomography is derived from the Greek word tomos which means "slice". t-arrival travel-time data is the goal of transmission travel-time tomography, so that velocity models that explain them can be obtained. It is an ill-posed inverse problem constrained by the available distribution of receiver in superface, (Bording et al., 1987).

14. **Variational calculus:** The calculus of variations deals with problems in which a function or curve is sought, rather than a value of some variable, that makes a given quantity stationary, usually an energy or action integral. Because a function is var-

ied, these problems are called variational. Variational principles, such as those of D'Alembert, Lagrange, and Hamilton, have been developed in classical mechanics; Fermat's principle (that of the shortest optical path) finds use in electrodynamics. Lagrangian variational techniques also occur in quantum mechanics and field theory, (Arfken and Weber, 1999).

Resumen

Título: Inversión de Tiempos de Arribo de Campos de Ondas Sísmicas PP y de Onda Convertida PS para la Estimación de un Modelo de Velocidades P y S del Subsuelo: Un Enfoque Level Set [*]

Autor: Carlos Andrés Niño Niño [**]

Palabras Clave: Tomografía sísmica, Ecuación eikonal, Level Set, Onda convertida PS, Estado adjunto, Fast Marching, Función de Green empírica, Teoría inversa, Modelos de velocidad de onda de corte V_s.

Descripción: La velocidad de onda cortante (V_s) es una propiedad fundamental de los medios elásticos cuya estimación a partir de ondas convertidas PS es desafiante y requiere modelar la interfaz donde ocurre la conversión de P a S. Este artículo presenta una tomografía PS donde los puntos de conversión/reflexión de ondas sísmicas corresponden al reflector geológico modelado con la función Level set en su nivel cero ($\phi(x, z) = 0$). El método propuesto pretende una inversión estable de V_s en un entorno de adquisición sísmica utilizando receptores multicomponente. Se utilizan modelos sintéticos que simulan verdaderos V_s, V_p y la ubicación del reflector geológico. Los tiempos de viaje de las ondas PS convertidas y las ondas PP reflejadas, tanto para datos observados como modelados (problema directo), se calculan utilizando la metodología propuesta por Rawlinson y Sambridge. Este método utiliza los tiempos de llegada de las ondas P desde la fuente sísmica hasta cada punto en el reflector como tiempos iniciales, que originan los tiempos T_{ps} y T_{pp}. Estos tiempos se determinan como soluciones a la ecuación eikonal mediante el método Fast

---

[*] Tesis Doctoral

[**] Facultad de Ingenierías Fisicomecánicas. Escuela de Ingenierías Eléctrica, Electrónica y de Telecomunicaciones. Programa académico. Director: PhD. Daniel Sierra Bueno. Codirector: PhD. Cesar Duarte. Codirector: PhD. William Agudelo.

Marching. La metodología plantea un funcional definido a partir de los residuales de los tiempos de viaje (modelados-observados), en función de las variables ϕ, V_s y V_p. Se propone minimizar el funcional utilizando el método de variaciones sobre el funcional aumentado, basado en el Lagrangiano asociado. La inversión toma los multiplicadores de Lagrange como variables adjuntas que actualizan las variables V_s, V_p, y $\phi(x, z)$, haciendo que los residuales de los tiempos se minimizen en cada iteración. El rendimiento del algoritmo se evalúa para modelos con geometrías de reflectores sinclinales, sinusoidales y monoclinas. La tomografía propuesta estima V_s y las posiciones de los reflectores, lo que puede contribuir a corregir las estáticas y mejorar la caracterización litológica de la superficie cercana.

Abstract

Title: Inversion of PP Seismic and PS Converted Wavefield Arrival Times for the Estimation of a Model of Subsurface P and S Velocities: A Level Set Approach. [*]

Author: Carlos Andrés Niño Niño [**]

Keywords: Seismic Tomography, Eikonal Equation, Level Set, Converted Wave PS, Adjoint State, Fast Marching, Empirical Green's Function, Inverse Theory, V_s Shear Wave Velocity Models.

Description: The shear wave velocity (V_s) is a fundamental property of elastic media, whose estimation from converted PS waves is challenging and requires modeling the interface where the P to S conversion occurs. This article presents a PS tomography where the conversion/reflection points of seismic waves correspond to the geological reflector modeled with the Level set function at its zero level ($\phi(x, z) = 0$). The proposed method aims for a stable inversion of V_s in a seismic acquisition environment using multi-component receivers. Synthetic models are used to simulate true V_s, V_p, and the location of the geological reflector. The travel times of converted PS waves and reflected PP waves, for both observed and modeled data (direct problem), are calculated using the methodology proposed by Rawlinson and Sambridge. This method uses the arrival times of P waves from the seismic source to each point on the reflector as initial times, which originate the times T_{ps} and T_{pp}. These times are determined as solutions to the eikonal equation using the Fast Marching method. The methodology proposes a functional defined from the residuals of the travel times

---

[*] Doctoral thesis

[**] Faculty of Physicomechanical Engineering. School of Electrical, Electronic, and Telecommunications Engineering. Academic Program. Director: Daniel Sierra Bueno. PhD. Co-director: Cesar Duarte. PhD. Co-director: William Agudelo, PhD.

(modeled-observed), as a function of the variables ϕ, V_s, and V_p. It is proposed to minimize the functional using the method of variations on the augmented functional, based on the associated Lagrangian. The inversion takes the Lagrange multipliers as adjoint variables that update the variables V_s, V_p, and $\phi(x, z)$, causing the time residuals to be minimized at each iteration. The algorithm's performance is evaluated for models with synclinal, sinusoidal, and monocline reflector geometries. The proposed tomography estimates V_s and the positions of the reflectors, which can contribute to correcting statics and improving the lithological characterization of the near surface.

Introduction

Problem Statement

The characterization of materials within a confined medium begins with the estimation of the transmission velocity of waves through the medium. This process is conventionally performed by a tomography algorithm that inverts the information given by the travel times of the waves, relating them to a predicted spatial model (Menke, 2012). This algorithm adjusts the velocities of the medium to obtain the times observed by sensors located in a given geometry. The purpose of the inversion is to minimize the difference between the observed times and those calculated from a spatial model of velocities. In the particular case of the seismic method, the sensors are located only on the surface, with a separation of the order of meters between them. This means that the measured wavefield is mainly composed of reflections, conversions and refractions with little spatial sampling. This limitation makes velocity estimation a very ill-posed problem.

Ill-posed inversion problems require the use of regularization methods to obtain stable solutions relative to the observed data. These methods introduce prior information about the solution, so that solutions that are outside the physically possible range for the materials under study are penalized. These methods include Tikhonov, total variation (TV), Laplacian and others. The disadvantage of these methods is that they smooth out changes in the medium, including reflectors.

Complementing the information delivered by V_p velocity models with V_s shear wave velocities generates a higher resolution seismic image of materials, allowing to contrast compositions of interest for Geophysics (Farfour and Yoon, 2016), which favors when analysis that data come from complex subsurface. The use of PS converted wavelet is proposed to determine S-wave traveltimes that allows implementing a tomography algorithm to estimate velocities V_s. PS converted wavelets are observed in greater detail in a multicomponent acquisition, where surface geophones have components in all three axial axes. The PS converted wave model requires a conversion surface which is proposed to be represented by the Level Set function ($\phi(x,z)$) (Wang et al., 2010), (Aghasi et al., 2011). This contour, together with the V_s and V_p models, is expected to be updated until they converge to the point of explaining the observed PS and PP times.

The following research question is posed:

How to pose a tomographic scheme that from the definition of interfaces estimates the propagation times of the converted wave PS and the PP, in order to obtain simultaneously P and S velocity models with discontinuities?

Question that conceives the following hypothesis:

From the study of reflections and conversions originated in a presumed interface defined by the Level Set contour, it is possible to pose and solve a tomographic scheme that allows the calculation of PP and PS converted wave times, for the construction of velocity models.

Justification

The development of a model of shear wave velocities S, in complement with information given by compressional waves P, allows to obtain an elastic model of mechanical properties of materials. In this sense, proposing a PS tomography algorithm improves the estimation of the composition of materials, obtaining images with better information to characterize a particular region under observation. Elastic maps show great utility in medical applications, such as the study of soft tissues (Hansen et al., 2015), as well as in geophysical characterization helping to obtain images of complex and deep subsurface (Farfour and Yoon, 2016), delineating reservoirs, gas clouds, pore overpressure prediction, among others.

The methodology proposed, for the modeling of V_s, is the use of the P-S converted wave traveltimes, as a basis for the implementation of the developed tomography algorithm. Consequently, data from a multicomponent acquisition are required. The P to S conversion is performed on the Level Set contour that models the geological reflector. So the proposed inversion, as the final tomography process, estimates a model of V_s simultaneously with the shape and depth of the reflector, as well as V_p if desired.

Outline of the Thesis Book

This thesis presents the results of the research on how a model of shear wave velocities S, V_s can be generated from the PS converted wave. Chapter 2 presents the state of the art on Tomography that aims to confront the reader with the different methodologies required for the development of the PS tomography algorithm proposed, as well as to situate it with the advances made by different studies in the path to obtain such models of V_s.

Chapter 3 presents the methodology followed to design the proposed PS tomography algorithm. The objective function (E) is the PS and PP time residuals that depend on the location and geometry of the reflector ($\phi(x, z)$), as well as on the slownesses corresponding to the P (S_p) and S (S_s) waves. In addition, using the variational calculation, the first variational of the objective function is determined, which is conditioned to the calculation of the variational of the PS-PP times. In the following subsections of chapter 3, a methodology is elaborated that uses the first Green's identity to obtain gradients over the entire space under study (Ω_1) from measurements on the contour (surface), which in addition to the use of Lagrange multipliers as adjoint operators, eliminates the computationally expensive PS-PP time variationals from the objective function variational.

Meanwhile, Chapter 4 describes for both the PS and PP fields, how the adjoints (Lagrange operators) should be, in order to eliminate from the equation of the first objective function variational the terms corresponding to the PS-PP time variationals. Chapter 5 describes in detail the created PS-PP tomography algorithm, as well as some considerations to be taken into account for the subroutines necessary for the global convergence of the proposed algorithm.

Finally, chapter 6 presents a numerical test to show how the PS-PP tomography algorithm works for different types of models. Subchapter 6.1 tests the tomography only by inverting the reflector modeled with $\phi(x, z)$ taking as known the velocity models V_s and V_p. Whereas, subchapter 6.2 inverts two parameters at the same time V_s and $\phi(x, z)$ taking as known the parameter V_p. The analogous test inverts V_p and $\phi(x,z)$ given as known V_s. These results are presented in section 6.3. While subchapter 6.4 presents the results when inverting all three parameters at once: $\phi(x,z)$, V_s and V_p.

Chapter 7 presents the discussion of the results as well as ideas that can improve the proposed tomography methodology. Finally, chapter 8 presents conclusions and recommendations of the study carried out to obtain the PS-PP tomography methodology.

Thesis main contribution

A novel strategy that estimates a model of S-wave velocities, as well as, the shape and depth of the reflector modeled with the Level Set function. The estimation of V_s is performed using the converted PS wave that is produced by the shock of the P-wave on the reflector that is modeled with the Level Set $\phi = 0$. The PS tomography methodology is developed for a seismic acquisition, sensors and sources at surface.

Regarding the formulation of this novel methodology the contributions are:

- A methodology for calculating the travel times of both PS converted waves and PP reflections simultaneously (forward problem). This strategy solves the eikonal equation using the fast marching algorithm. The algorithm calculates the travel times from source to reflector ($\phi = 0$), so that the arrival times above $\phi = 0$ are established. These times above $\phi = 0$ are taken as sources emitting waves (PS, PP) in the direction of the surface, the fast marching algorithm evaluates the travel times.

- The design of adjoint operators that allow to obtain gradient updates of the variables to be estimated: V_s, V_p and reflector: $\phi = 0$. The adjoints are made from the gradients determined from the first variational of the objective function, defined using the time residual between the observed times PS-PP and those measured on the velocity model V_s and V_p, over Ω_1 bounded region by the level set function ($\phi = 0$). So the inversion can be solved, equivalent to the forward problem, using the adjoint operators.

- A strategy to tune the parameters of the PS-PP tomography equations developed to maximize performance, in terms of convergence of V_s and V_p velocities and different reflector geometry. The performance is promising for different reflector geometries.

1. Objectives

In this part of the study, the established objectives are described with the purpose of addressing the posed research question..

1.1. General Objective

Determine seismic wave arrival conditions on the contour defined by the Level Set as a methodology to perform PS and PP converted wave tomography for the construction of a P- and S-wave velocity model.

1.2. Specific objectives

- Estimate the direction of propagation of the converted PS wave by identifying angles of incidence and emergence at the conversion point on the seismic interface modeled by the geometry of the level set contour.

- Formulate a PP tomography scheme using the given emergence angle at the PS conversion point on the level set contour to estimate travel times from reflection to surface.

- Propose a methodology to invert traveltimes of PP and PS waves jointly, allowing to obtain P and S velocity models from the interface evolution given by level set.

2. State of the art

The current development of PS-converted wave tomography involves a registration process in the time domain of PP and PS waves, a procedure that allows the location of a reflector to be determined in this domain. Here, the tomography simultaneously adjusts the S and P velocities to obtain the depth of the reflector. The complexity of the challenge has been demonstrated in several studies Mathewson et al. (2013), Stewart et al. (2002), Farfour and Yoon (2016), Hardage et al. (2011) and Li and Zhang (2011), where it is shown that current methods for estimating V_s in conjunction with V_p are complicated and subjective, relying on the experience of the analyst. Therefore, there is a need to develop an algorithm that incorporates the reflector in space by varying its shape and depth in the inversion process as a variable to perform the estimation of V_s in conjunction with V_p.

Converted PS-waves are generated at interfaces that exhibit contrasting physical properties of the medium. Therefore, it is essential to incorporate a proper mathematical representation of the interface into a complete inversion formulation for $V_p(x, z)$ and $V_s(x, z)$ based on converted PS waves. In this study, we introduce a new framework in seismic tomography, using both reflected PP-waves and converted PS-waves on the reflector. Inversion process that requires the spatial representation of the potential location of the common reflection/conversion point for PP and PS waves by representing the interface as a zero contour defined by level set theory. The method presented here focuses exclusively on the kinematics of the PS-PP waves, excluding their dynamic characteristics (i.e. amplitudes).

We define an objective function that establishes a relation between the model variables (medium velocity fields and reflector position) and the travel time residuals of the reflected PP and converted PS waves. This paper focuses on the study of a single interface case. However, the proposed methodology is versatile enough to be extended to models with multiple interfaces.

2.1. Theoretical Framework

Previous work on the estimation of shear wave V_s and compression V_p velocity models from PS conversions and PP reflections has used two main methodologies: normal moveout (NMO) and Pre-stack depth migration (PSDM). NMO Methodology estimates coefficients to flatten the curves described by PS and PP travel times, parameterized as a polynomial model, from data acquired at the surface, estimating initial models of the converted wave $V_{ps}(x, z)$, as well as $V_p(x, z)$ velocities. As a second stage, a registration process considers the depth mistmatch between the events of reflections PP and PS conversions as an input for estimating shear wave velocity $V_s(x, z)$, having as reference the P wave and converted wave times. PS and PP travel time curves from seismic acquisitions of complex (and possibly anisotropic) subsoil are discontinuous, complex to identify, degrading the NMO reliability and the recording quality, providing thus inaccurate models of $V_s(x, z)$.

The implementation of new methodologies to strengthen the registration process, such as the one proposed in (Fomel and Backus, 2003), where they use a warping function that estimates a correlation model of PS converted wave and PP compressional images, achieve higher accuracy in assessing $V_s(x,z)$ models by aligning the PS reflectors with the PP reflectors.

On the other hand, several authors have followed a PSDM processing that performs a depth migration of the gathers so that PP reflections and PS conversions are spatially located at their real coordinates in depth. Having the V_p model with the PP reflection events as reference, $V_s(x,z)$ models achieved with the NMO-Registration workflow are iteratively improved by flattening the PS events observed in the gathers in depth.

The development of a PS tomography to compute V_s, which includes within the inversion process the location and shape of the reflector as well as the variation of the velocity model V_p, allows establishing a mismatch function between observed and modeled first arrival travel times for both PS conversions and PP reflections; allowing to jointly invert V_s/V_p ratio as well as the location and shape of the reflector. Having an accurate V_s/V_p ratio model allows the elasticity of the subsurface materials to be characterized.

In this vein, (Mathewson et al., 2013) proposes a joint PP/PS tomography algorithm with floating event constraints, which attempts to produce flat events for both PP and PS in the Gather at Depth (PSDM), while at the same time seeking to match the depths of equivalent PP and PS events.Therefore, the authors recommend including a depth constraint.

In this doctoral thesis, the main contribution of which has been submitted for publication to JGI journal (Niño et al., 2023), the level set method is adopted (Osher and Fedkiw, 2005) as a model for the interface geometry. To include a depth constraint, the level set technique for a P field is introduced by Cameron et al. (2007); they perform a time-depth conversion process, using the $\phi(x, z) = 0$ as a reflector formulation that shifts the reflections observed in the seismic data to the correct locations in the depth space (x, z). Wang et al. (2010) propose the use of the level set as a complement to the Tikhonov regularisation. Level Set at its zero level $\phi(x, z) = 0$ maps an interface that precisely defines an electrical impedance change. This approach produces a stable and more accurate electrical impedance tomography. Aghasi et al. (2011) study the use of the level set in inverse problems and presents dimensionality reduction by using radial basis functions to parameterize the level set function, which increases the stability of the inversion process.(Prieto and Dorn, 2016) use the level set regularisation strategy to reconstruct the absorption and scattering properties in diffuse optical tomography for brain imaging. They suggest using scattering promotion to regularise the velocity model to reduce the sensitivity of the data within the brain. Results show high accuracy but low flexibility when the surface under study includes more than one type of scattering point.

Zheglova and Farquharson (2012) present the use of level set in seismic inversion problems. They use it to reconstruct the sharp boundary between two known slowness models from cross-borehole acquisition data, from which they extract the transmitted P-wave first arrival times. Experiments on synthetic data demonstrate the strategy works well on recovering the current model. In the same approach, Li and Leung (2013) implement a methodology of tomography of first arrivals of P transmitted waves between sources and receivers in opposite positions, including in the inversion process the position and shape of the reflector using the Level Set function with its zero level $\phi(x, z) = 0$, obtaining thus V_p models and the interface. Li et al. (2014) present the application of level set in a Crosswell seismic tomography using residual times of reflected and transmitted waves, using the reflector modeled with $\phi(x, z) = 0$ as the reflection surface. The solution of the update factors makes use of the back-propagated residual times throughout the medium using the partial differential equations (PDEs) represented by the adjoint equation of state.

Kadu et al. (2016) and Dorn and Wu (2021), use radial basis functions to parameterize the level set function in full-wave inversion problems where the contour $\phi_{(x,z)} = 0$ maps the boundaries of a salt body of known density. Lamert et al. (2018) perform elastic full-waveform inversion by using level set to predict areas of perturbation.

Notice that the tomography methodologies implemented in seismic inversion problems make use of an acquisition geometry that allows including information of transmitted waves, such as the cross borehole geometry(sources and sensors in opposite planes) as in (Zheglova and Farquharson, 2012) or (Li et al., 2014) where sensors are located in the same plane, but in an opposite boundary of the sources (Crosswell), thus allowing to add information of reflection waves. In contrast, as a novelty in this doctoral thesis, not alike the cross-well acquisition where transmitted waves are used to perform the inversion process, the data observed to develop the proposed methodology of PS-PP tomography are obtained from an acquisition geometry where the sources and receivers are on the free surface (conventional seismic), limiting the proposed tomography to the measurement of the first arrival times of the converted (PS) and reflected (PP) waves on the reflector modeled with the level set function ($\phi(x, z) = 0$). Thus, in the absence of transmitted waves, the simultaneous estimation of V_s and V_p is proposed.

In this doctoral thesis, modeled PS and PP times are computed using the Fast Marching Methodology proposed by Rawlinson and Sambridge (2005) to solve the Eikonal equation from the Level set $\phi(x, z) = 0$ geological reflector model.

The construction of an inverse framework system to estimate models of V_s and V_p is significantly complex. Some authors have implemented a gradient type optimization method Zheglova and Farquharson (2012) to perform a tomography process where V_p is known and the location and shape of the interface is searched using $\phi(x, z) = 0$ from the transmitted travel times. Here, the perturbation method is used, offering an optimization strategy as in Li et al. (2014) so that together with the Level Set methodology and the variational analysis, an algorithm is elaborated that allows estimating the location of the geological reflector and the simultaneous estimation of V_s and V_p.

The solution for the misfit function variational is achieved by devising adjoint operators that are implemented through PDEs to keep computational cost similar to a forward-modeling problem, as in (Huang and Bellefleur, 2012),(Taillandier et al., 2009),(Leung and Qian, 2006) and (Zheglova and Farquharson, 2012). The design and implementation of this algorithmic framework is described in detail in the following sections.

2.2. The converted PS wave tomography problem

The acquisition of multicomponent seismic data (MCS) allows the capture of vectorial movements of mechanical vibration in three cartesian axes, in such a way that it can separate the different polarizations of the wavefield, allowing thus to better distinguish the times of first arrivals of the converted wave PS, T_{ps}, generally with most of its energy in the radial component (Figure 1 -a curved events in red); and in the same way, for PP reflections times, T_{pp}, in vertical component (Figure 1 -a hyperbolic events in blue). Figure 1 -b represents for a Shot S_i induced by the activation of a P wave source (red star), located at (x_{si}, z_{si}), the propagation of the wave. P source-reflector is represented by means of a ray (black dotted line) that is transmitted from the source to a point of conversion-reflection on the geological reflector, generating a PS ray (solid red line) and a PP ray (solid blue line), which travel to the free surface receptors at Γ where the PS-PP waves are acquired. Thus, Figure 1 synthesizes the physical behavior of the converted PP and PS reflection waves traveling respectively with V_p and V_s velocities for a multicomponent seismic acquisition geometry; the travel times of first arrivals, Tps and Tpp, with red and blue curved events are identified in the horizontal and vertical Gathers.

In this doctoral thesis, the use of the Level Set function $\phi(x, z)$ as a geometric description of the space Ω, of which the level $\phi(x, z) = 0$ models the reflector R, where the conversion points PS and reflection PP are located, as shown in Figure 2, is proposed and developed. The Level Set function may be defined as a function of distances (either positive or negative depending of the region) from a level zero ($\phi(x, z)$, in Figure 2), which divides space Ω into two subspaces Ω_1 ($\phi(x, z) \leq 0$) and Ω_2 ($\phi(x, z) > 0$) (Osher and Fedkiw, 2005). Starting from $\phi(x, z) = 0$, properties are defined for the $\Omega 1$ region: velocities V_{p1} and V_{s1}, mathematically the equation (1) makes the assignment using Heaviside function $H(\phi)$, ((Prieto and Dorn, 2016),(Zheglova and Farquharson, 2012),(Li et al., 2014) and (Aghasi et al.,

Figure 1

Correspondence between waves captured by multicomponent receivers at the surface Γ and the PS conversions and PP reflections occurring at the geological reflector, R, for a $shot_i$ *from the source at the red star.*

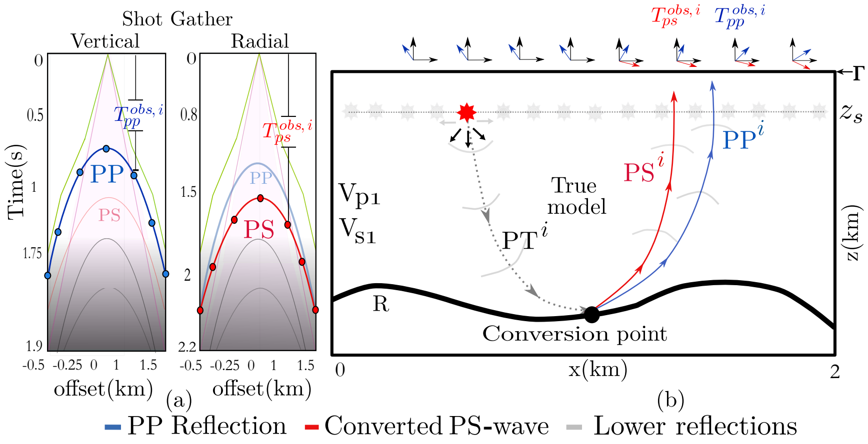

(a) Travel times for the first arrivals of PS waves (red) and PP waves (blue) for a rotated (vertical, radial) multicomponent acquisition. (b) Rays generated by the activation of $shot_i$ *at the location marked by the red star: P transmission waves (gray dotted line), PP reflected wave (blue line), and PS converted wave (red line)..*

2011)), definition that allows the seismic tomography process to be carried out by estimating the velocities of the medium by subregions. Equation (1) expresses the velocities $V(x,z)$ in Ω parameterised by the fields $V_1(x,z)$ and $V_2(x,z)$. By updating $\phi(x,z)$ and $V_1(x,z)$, subspace Ω_1 can be modified along with $V(x,z)$ in such subspace. Ω_2 varies accordingly to meet $\Omega_1 \cup \Omega_2 = \Omega$ and $V_2(x,z)$ can be kept unvaried on the new Ω_2:

$$V(x,z) = V_1(x,z)(1 - H(\phi(x,z))) + V_2(x,z)H(\phi(x,z)), \quad (x,z) \in \Omega. \tag{1}$$

The contour $\phi(x,z) = 0$ simulates the effect of the geological reflector R where the P-wave, produced by the seismic source impinging, generates PS conversion and PP reflection

Figure 2

Tomography spatial model representation of PS converted wave and PP reflection using the Level Set methodology, which by means of the $\phi(x,z) = 0$ level models the true reflector.

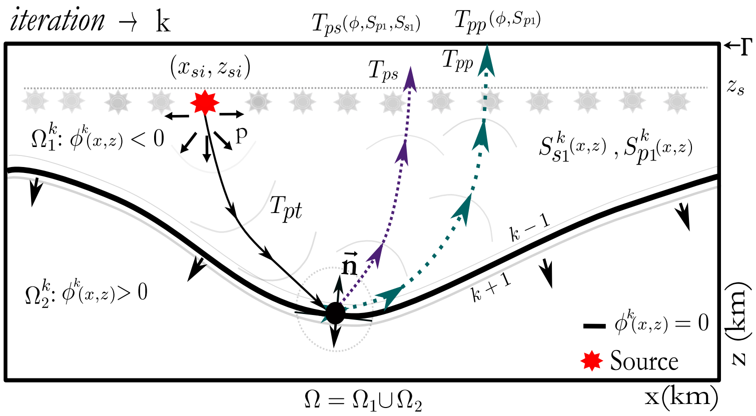

The level $\phi^k(x,z) = 0$ divides the Ω space into two subspaces, $\Omega 1$ and $\Omega 2$, each space with different physical properties: for shear waves slowness Ss, while for compressional slowness Sp. The reflector model $\phi(x,z) = 0$ evolves at each iteration to the true reflector. The image also shows a vector normal to $\phi(x,z) = 0$, $\vec{n}$, which serves as a reference for the calculation of the angle of incidence and reflection of the P-wave and such as the PS conversion on the reflector model.

waves following Snell's law: $\frac{sin(\theta)}{Vp} = \frac{sin(\alpha)}{Vs}|_{\phi(x,z)=0}$, see Figure 2 . The P-wave produced by the seismic source travels with time T_{pt} to the reflector modeled by $\phi(x,z) = 0$, where the energy is partitioned in converted PS and reflected PP waves and travels to multicomponent receivers on the Γ surface. The arrivals T^i_{ps} and T^i_{pp} are determined numerically by solving the eikonal equation (2) for each shot $S_i|i = 1, 2, ..., N$. The PS-PP tomography methodology presented in this doctoral thesis aims at estimating the models $V_{p1}(x,z)$ and $V_{s1}(x,z)$ in the region Ω_1, by minimizing the residual of times between the arrivals T^i_{pp} and T^i_{ps} calculated from the models $V_{s1}(x,z)$ and $V_{p1}(x,z)$ and the observed times $T^{obs,i}_{ps}$ and $T^{obs,i}_{pp}$ represented by the red and blue PS-PP curved events in the Figure 1 -a Gathers. The simultaneous PS-

PP Tomography methodology at iteration k has as outputs $\phi^k(x,z)=0$, V_s^k and V_p^k, take into account the interaction between all three variables during the inverse processing. The variable $S(x,z)=\frac{1}{V(x,z)}$, reciprocal of the velocity defined as the slowness of the medium, is a nomenclature used for numerical simplicity in the eikonal equation (2).

$$|\nabla T(x,z)| = \frac{1}{V(x,z)} = S(x,z), \quad (x,z) \in \Omega_1 \setminus (x_s,z_s), \qquad T(x_s,z_s)=0. \tag{2}$$

At the end of the proposed tomography process, the set of contour levels, in each iteration, is expected to k, $\phi^k(x,z)=0|k=1,2,\ldots,end$ tend to converge to the physical geological reflector R (Figure 2), and $V_p^{k=end}(x,z)$ and $V_s^{k=end}(x,z)$ to the physical V_p and V_s velocity models, a process described in Figure 3 . A mathematical proof of this convergence is not provided yet, and even it is possible that the convergence is restricted to a limited favorable model/acquisition space. However, in section 6, numerical tests demonstrate that for some representative case, this general convergence is a reasonable assumption.

Figure 3

PS-PP tomography methodology at iteration k for shot$_i$.

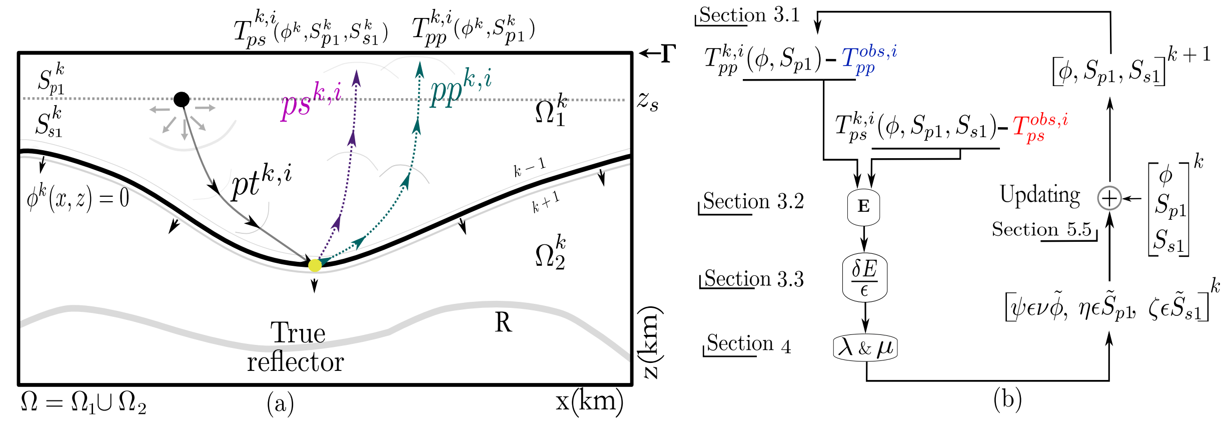

(a) Modeled rays generated by shot$_i$ *for reflected PP-wave (green) and converted PS-wave (purple) at modeled reflector for iteration k (*$\phi^k(x,z)=0$*). As iterations progress, modeled rays should converge to true PP (blue) and PS (red) rays. (b) Inversion process based on the design of* λ *and* μ *fields in order to minimize PS-PP time residuals by optimally updating model parameters* $\phi(x,z)$ *and slowness fields,* $S_s(x,z)$ *and* $S_p(x,z)$*.*

3. Proposed first arrival tomography PS conversion PP reflection algorithm using a Level Set $\phi(x,z)$ interface model

The PS-PP tomography algorithm iteratively estimates slowness models, $S_{s1}(x,z)$ and $S_{p1}(x,z)$, on a region Ω_1, along with the boundary of this region, which corresponds to an interface modelled with the Level Set function at its level $\phi(x,z) = 0$ (Figure 3.a). The illumination of region Ω_1 is achieved by the sequential activation (at time $t = 0$) of N P-wave sources (Shot$_i$, with $i = 1, 2, \ldots, N$) positioned at a depth (z_s) below the free surface Γ (a sample source is represented by the black dot in Figure 3.a).

The algorithm computes at iteration k the times $T_{ps}^{k,i}(x,z)$ and $T_{pp}^{k,i}(x,z)$ for each Shot$_i$. This allows the definition of residual times with respect to the observed times $T_{ps}^{obs,i}$ and $T_{pp}^{obs,i}$. This information is used to design adjoint states for each $Shot_i$, which are added up for all N-$Shots$ to define a gradient that updates $S_{s1}^{k}(x,z)$, $S_{p1}^{k}(x,z)$, and $\phi^k(x,z) = 0$ aiming to decrease the residual times on next iteration $k+1$.

In this process, we reformulate the PS-PP arrival times in terms of variables $S_{s1}^{k}(x,z)$, $S_{p1}^{k}(x,z)$, and $\phi^k(x,z)$ for each $Shot_i$, i.e., $T_{pp}^{k,i}(\phi^k, S_{p1}^k)$ and $T_{ps}^{k,i}(\phi^k, S_{p1}^k, S_{s1}^k)$. From this reformulation, the inversion strategy estimates perturbations that modify the initial variables to minimize residual times. We adopt a variational formulation to estimate the adjoint fields that determine the optimal perturbations $\tilde{\phi}(x,z)$, $\tilde{S}_{p1}(x,z)$, and $\tilde{S}_{s1}(x,z)$. Figure 3.b summarizes each of the steps and the section in the article where they are detailed.

3.1. Forward problem: Calculation of travel times $T_{pp}(\phi, S_{p1})$ and $T_{ps}(\phi, S_{p1}, S_{s1})$ on $S_{p1}(x,z)$ and $S_{s1}(x,z)$ models defined by $\phi(x,z)$

The proposed algorithm for solving the forward problem in PP-PS tomography is based on the Fast Marching Methodology (FMM) (Treister and Haber (2016); Hassouna and Farag (2007)), which solves the Eikonal equation to compute travel times: $T_{pp}(\phi^k, S_{p1}^k)$ and $T_{ps}(\phi^k, S_{p1}^k, S_{s1}^k)$. The PS-PP tomography is formulated for a geological layer Ω_1. So, the fields $S_{s1}(x,z)$ and $S_{p1}(x,z)$ are bounded by the zero level of the function $\phi(x,z)$. This is expressed as $S_{s1}(x,z)(1 - H(\phi(x,z)))$ and $S_{p1}(x,z)(1 - H(\phi(x,z)))$ for all points (x,z) in the domain Ω. Throughout the tomography process, the values of $S_{s2}(x,z)H(\phi(x,z))$ and $S_{p2}(x,z)H(\phi(x,z))$ remain unchanged.

Figure 4.a illustrates the propagation of P-waves within medium Ω_1, characterized by slowness S_{p1}, upon activation of the source (the black point that indicates the origin of the shot at t=0). The wave trajectory is depicted by a solid dark grey ray. Travel time $T_{pt}(\phi, S_{p1})$ is computed using the Fast Marching Method (FMM), which numerically solves the Eikonal Equation (3). As a result, the P-wave arrives on $\phi(x,z) = 0$ with an angle θ_t and PS conversions and PP reflections take place with elevation angles α and θ_r, respectively. These angles are constrained by Snell's law: $\frac{sin(\theta_t)}{V_p} = \frac{sin(\theta_r)}{V_p} = \frac{sin(\alpha)}{V_s}|_{\phi(x,z)=0}$. The determination of these angles, as shown in Figure 4.b, involves computing the gradient of the arrival times at $\phi(x,z) = 0$.

Figure 4

The propagation of travel time across the geometry is presented: Direct problem for PP-PS fields at iteration k and shot$_i$. The scheme illustrates how the Fast Marching Method (FMM) is used to calculate travel times, with the location of the source (black point) serving as the starting point (time zero).

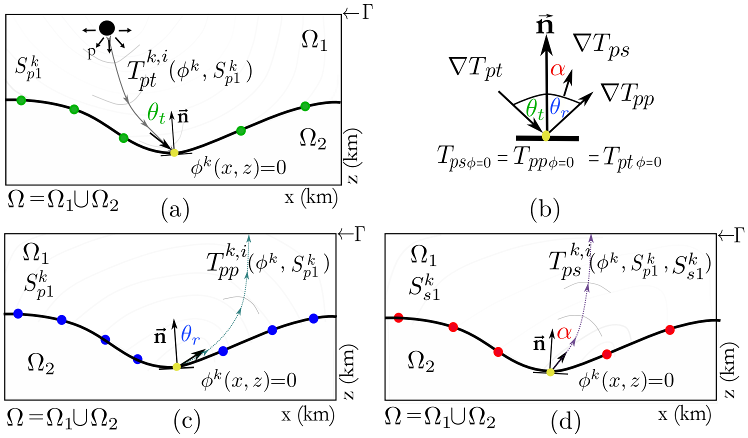

(a) Travel times of transmitted waves T_{pt}. (b) Boundary condition on $\phi(x,z)=0$ for the travel times of PT waves with PS-PP waves, along with the angle relationship determined by the gradient of the travel times: θ_t (in green) represents the arrival angle at the reflector, α (in red) indicates the angle of the converted PS wave, and θ_r (in blue) corresponds to the angle of the reflected PP wave. (c) Travel times of reflected waves T_{pp}. (d) Travel times of converted waves T_{ps}.

$$
\begin{gathered}
|\nabla T^{k,i}_{pt}(\phi^k, S^k_{p1})| = S^k_{p1}(x,z), \quad (x,z) \in \Omega^k_1 \setminus (x^i_s, z^i_s) \\
T^{k,i}_{pt}(x^i_s, z^i_s) = 0, \quad i = 1,2,...,N.
\end{gathered}
\tag{3}
$$

In order to compute travel times, we follow the methodology RS-FMM proposed in Rawlinson and Sambridge (2005), where all the points of the reflector ($\phi(x,z)=0$) are considered as secondary sources. The Eikonal equation (4) relates $T_{pp}(\phi, S_{p1})$ and the propagation slowness model $S_{p1}(x,z)$, considering that the initial travel time is the arrival time $T_{pt}(\phi, S_{p1})$ at each point on $\phi(x,z)=0$. Thus, we obtain the arrival times at Γ surface, $T^i_{pp}(\phi, S_{p1})$, see the detailed geometry in Figure 4 .c where the dashed green/blue ray models the PP reflection.

$$\begin{aligned} |\nabla T_{pp}^{k,i}(\phi^k, S_{p1}^k)| &= S_{p1}^k(x,z), \quad (x,z) \in \Omega_1^k \\ T_{pp}^{k,i}(\phi^k, S_{p1}^k) &= T_{pt}^{k,i}(\phi^k, S_{p1}^k), \qquad (x,z) \; on \; R: \phi^k(x,z) = 0. \end{aligned} \tag{4}$$

From the gradient $\nabla T_{pp}(\phi, S_{p1})$, the angle of reflection θ_r, with respect to the normal of the reflector, can be calculated. The inset in Figure 4.b shows the correspondent geometric relationship. In this case, θ_r is equal to the incident angle θ_t of the transmitted P-wave, as the propagation medium is modeled with the same $S_{p1}(x,z)$: $\theta_t = \theta_r$.

For the calculation of PS conversion travel times $T_{ps}(\phi, S_{p1}, S_{s1})$ (geometry described in Figure 4.d), we verify in Niño et al. (2022) that the methodology proposed by Rawlinson and Sambridge (2005) can also be applied with the PS field. This test is performed by comparing the times calculated with ray theory on each point of the reflector and the RS-FMM methodology. We find a negligible difference between the PS travel times calculated with those techniques. The RS-FMM algorithm is chosen for its lower computational cost.

$$\begin{aligned} |\nabla T_{ps}^{k,i}(\phi^k, S_{p1}^k, S_{s1}^k)| &= S_{s1}^k(x,z), \qquad (x,z) \in \Omega_1^k \\ T_{ps}^{k,i}(\phi^k, S_{p1}^k) &= T_{pt}^{k,i}(\phi^k, S_{p1}^k), \quad (x,z) \; on \; R: \phi^k(x,z) = 0. \end{aligned} \tag{5}$$

To solve the Eikonal equation 5, we use as initial times $T_{pt}^{i}(\phi, S_{p1})$ at $\phi(x,z) = 0$. The conversion angle α of the S-field (Figure 4.d) can be calculated by considering the angle between the gradient $\nabla T_{ps}^{i}(\phi, S_{p1}, S_{s1})$ and the normal of the reflector. This allows us to establish residual travel times for both the PS and PP propagation fields ($R_{ps}^{k,i}$ and $R_{pp}^{k,i}$) for each $shot_i$, utilizing the observed PS-PP times by the receivers at Γ, as depicted in Figure 3:

$$\boldsymbol{R}_{ps}^{k,i} = T_{ps}^{k,i}(\phi^k, S_{p1}^k, S_{s1}^k) - T_{ps}^{obs,i}, \qquad \boldsymbol{R}_{pp}^{k,i} = T_{pp}^{k,i}(\phi^k, S_{p1}^k) - T_{pp}^{obs,i}. \tag{6}$$

3.2. Minimization of misfit function: variational formulation

L2 norm is widely used to quantify the misfit between computed and observed travel times. For instance, in the context of a Crosswell acquisition geometry, (Li et al. (2014)) successfully estimate S_p field to minimize the L2 norm of the PP time residuals.

For the proposed PP-PS tomography, the misfit function $E(\phi, S_{p1}, S_{s1})$ is computed for each $shot_i$[1], by solving the forward problem described in the previous section, as::

$$E(\phi^k, S_{p1}^k, S_{s1}^k) = \frac{1}{2}\sum_{i=1}^{N}\left(\int_{\partial\Omega=\Gamma} |T_{ps}^{k,i}(\phi^k, S_{p1}^k, S_{s1}^k) - T_{ps}^{obs,i}|^2 ds + \int_{\partial\Omega=\Gamma} |T_{pp}^{k,i}(\phi^k, S_{p1}^k) - T_{pp}^{obs,i}|^2 ds\right). \tag{7}$$

In order to find a physical realisation of the initial model parameters, a perturbation of such patameters is introduced: $\phi(x,z)+\epsilon\nu\tilde{\phi}(x,z)$, $S_{s1}(x,z)+\epsilon\tilde{S}_{s1}(x,z)$ and $S_{p1}(x,z)+\epsilon\tilde{S}_{p1}(x,z)$. The

---

[1] The $\sum_{i=1}^{N}$ indicates that the functional must be computed for N shots. Each shot generates P-waves, which travel to the reflector, where they are reflected and converted into PP-PS waves. The sequential scanning of the shots illuminates the Ω region from different shot locations, so that the subsurface image will be the aggregation of the information obtained from each shot. This process is illustrated in Figure1.b

search for appropriate perturbations is carried out by formulating the first variation of the misfit function using the Gâteaux variation: $\frac{\delta E}{\epsilon} = \frac{[E(\phi+\epsilon\nu\tilde{\phi}, S_{p1}+\epsilon\tilde{S}_{p1}, S_{s1}+\epsilon\tilde{S}_{s1})-E(\phi, S_{p1}, S_{s1})]}{\epsilon}$,where ϵ controls the step size in the search direction, a critical consideration for all sufficiently small ϵ, similar to the concept of directional derivative. In this context, Leung and Qian (2006) apply this variational approach in the same sense as the gradient descent method, where $\frac{\delta E}{\epsilon} \leq 0$ is a necessary condition to find the minimum of the energy functional E:

$$\frac{\delta E}{\epsilon} = \sum_{i=1}^{N} \left(\int_{\Gamma} (\widetilde{T}_{ps}^{k,i}(T_{ps}^{k,i}(\phi^k, S_{p1}^k, S_{s1}^k) - T_{ps}^{obs,i}))ds + \int_{\Gamma} (\widetilde{T}_{pp}^{i}(T_{pp}^{k,i}(\phi^k, S_{p1}^k) - T_{pp}^{obs,i}))ds \right) \leq 0. \tag{8}$$

Equation (8) establishes the dependence on travel time variations $\widetilde{T}_{ps}$ and $\widetilde{T}_{pp}$. The derivation of this variational equation δE is given in Appendix A (equations (45) to (47)).

3.3. Inverse problem: Eikonal variational equation for the design of adjoint operators

The first variational of the objective function, given by equation (8), involves the calculation of both residuals of PS-PP travel times and the variationals $\widetilde{T}_{ps}$ and $\widetilde{T}_{pp}$. For instance, in the PS field case: $\epsilon\widetilde{T}_{ps} = T_{ps}(\phi + \epsilon \cdot \nu\widetilde{\phi}, S_{p1} + \epsilon \cdot \widetilde{S}_{p1}, S_{s1} + \epsilon \cdot \widetilde{S}_{s1}) - T_{ps}(\phi, S_{p1}, S_{s1})$. In order to reduce the high computational cost of these types of operations, it's possible to replace $\widetilde{T}_{ps}$ and $\widetilde{T}_{pp}$ with adjoint state variables, derived from the residual times in (6), as demonstrated in various studies as Leung and Qian (2006), Zheglova and Farquharson (2012) and Taillandier et al. (2009). These variables, as stated in Plessix (2006), perform the inversion without directly calculating $\widetilde{T}_{ps}$ and $\widetilde{T}_{pp}$, thus turning the inverse problem into a direct one, by backpropagating the residual times of the PS-PP fields (Equation (6)) throughout all Ω_1. From these adjoint states, the optimal perturbations $\tilde{\phi}(x,z)$, $\tilde{S}_{p1}(x,z)$, and $\tilde{S}_{s1}(x,z)$ can be estimated to update $S_{p1}(x,z)$, $S_{s1}(x,z)$ and $\phi(x,z)$, so that the residual times are reduced at each iteration.

So, the variationals $\widetilde{T}_{ps}$ and $\widetilde{T}_{pp}$ are replaced by adjoint state variables described in terms of the optimal perturbations $\tilde{\phi}(x,z)$, $\tilde{S}_{p1}(x,z)$, and $\tilde{S}_{s1}(x,z)$, which update the models $S_{p1}(x,z)$, $S_{s1}(x,z)$, and $\phi(x,z)$ so that the residual PP-PS times are reduced at each iteration (k).

Since the eikonal Equations ((3), (4), and (5)) act as a constraint, coming from the physics of wave propagation on Ω_1 (for the PS field, $\int_{\Omega} g_{ps}(\phi, S_{p1}, S_{s1})d\Omega = \int_{\Omega_1}(S_{s1} - \nabla T_{ps}\nabla T_{ps}(\phi, S_{p1}, S_{s1})d\Omega = 0)$, these can be used to formulate a Lagrangian multipliers equation which aims to incorporate the constraints into the objective function. For the PS field, the augmented functional in terms of the Lagrange multiplier λ can be defined as: $\mathcal{L}(\phi, S_{p1}, S_{s1}, \lambda) = E(\phi, S_{p1}, S_{s1}) - \int_{\Omega} \lambda g_{ps}(\phi, S_{p1}, S_{s1})d\Omega$. It is then proposed to compute the augmented variational function $(\frac{\delta\mathcal{L}(\phi,S_{p1},S_{s1},\lambda)}{\epsilon} = \frac{\delta E}{\epsilon} - \int_{\Omega} \lambda \frac{\delta g_{ps}(\phi,S_{p1},S_{s1})}{\epsilon} d\Omega)$, known as the adjoint equation, which is used to solve the minimisation of the PP-PS travel time residuals. In this sense, it is necessary to formulate the variational of the eikonal equations, which can be computed from the difference between the eikonal equation for times with perturbation, $T + \epsilon\widetilde{T}$ (Equation (9)), and the eikonal equation for times without perturbation, T (Equation (10)), presented here for the PS field but extendable to the PP field.

$$(\nabla T_{ps}(\phi, S_{p1}, S_{s1}) + \epsilon \nabla \widetilde{T}_{ps}))^2 = S_s^2(\phi + \epsilon \nu \widetilde{\phi}, S_{s1} + \epsilon \widetilde{S}_{s1}, S_{s2}) \tag{9}$$

$$\nabla T_{ps}^2(\phi, S_{p1}, S_{s1}) = S_s^2(\phi, S_{s1}, S_{s2}) \tag{10}$$

The specifics of these developments can be found in the appendix equations (48)-(49). This process results in equation (11). It is important to mention that both equations depend on $\nabla \widetilde{T}_{ps}$ and $\nabla \widetilde{T}_{pp}$, the equations are only identified for the PS field.

$$2\epsilon \nabla \widetilde{T}_{ps}(\nabla T_{ps}(\phi, S_{p1}, S_{s1})) + \mathcal{O}(\epsilon^2) = S_s^2(\phi + \epsilon \cdot \nu \widetilde{\phi}, S_{s1} + \epsilon \cdot \widetilde{S}_{s1}, S_{s2}) - S_s^2(\phi, S_{s1}, S_{s2}) \ . \tag{11}$$

In order to develop the velocity variation shown on the right hand side of equation (11), it is necessary to smooth the discontinuity present in the Heaviside step function, which is defined by the location of $\phi(x, z) = 0$, based on the representation using ϕ as shown in equation (1). The processes described in Álvarez and Coutinho (2013), Tsai and Osher (2005) and Li and Leung (2013) can be used to perform this type of smothing given by a shape parameter τ $(0 < \tau < 1)$. It determines the resolution of the reflector and allows the calculation of derivatives in this range. The definition of $H_\tau(\phi)$ is shown in the equation (50). The appendix equations (51) to (53) contain the complete calculations of the variations of the velocities described on the right-hand side of equation (11).These calculations yield the result shown below:

$$2\epsilon\nabla\widetilde{T}_{ps}(\nabla T_{ps}(\phi, S_{p1}, S_{s1}))+\mathscr{O}(\epsilon^2) = 2\epsilon S_s(\phi, S_{s1}, S_{s2})\left(\nu\widetilde{\phi}\frac{S_{s2}-S_{s1}}{2\tau\cosh^2(\frac{\phi}{\tau})}+\widetilde{S}_{s1}[1-H_\tau(\phi)]\right)+\mathcal{O}(\epsilon^2) \tag{12}$$

For simplicity of notation we define:

$$A_s = S_s(\phi, S_{s1}, S_{s2})\frac{(S_{s2}-S_{s1})}{2\tau\cosh^2(\phi)}, \tag{13}$$

$$B_s = S_s(\phi, S_{s1}, S_{s2})[1-H_\tau(\phi)] \tag{14}$$

$$A_p = S_p(\phi, S_{p1}, S_{p2})\frac{(S_{p2}-S_{p1})}{2\tau\cosh^2(\phi)}\ , \tag{15}$$

$$B_p = S_p(\phi, S_{p1}, S_{p2})[1-H_\tau(\phi)] \tag{16}$$

Thus, the first variational of Eikonal equations (4) and (5) are summarized as:

$$\nabla\widetilde{T}_{ps}\cdot\nabla T_{ps}(\phi, S_{p1}, S_{s1}) = \overbrace{A_s\nu\widetilde{\phi}+B_s\widetilde{S}_{s1}}^{w_{ps}} \tag{17}$$

$$\nabla\widetilde{T}_{pp}\cdot\nabla T_{pp}(\phi, S_{p1}) = \overbrace{A_p\nu\widetilde{\phi}+B_p\widetilde{S}_{p1}}^{w_{pp}} \tag{18}$$

In Equation (19), based on Equations (17) and (18), the augmented variational functional

$(\delta\mathcal{L}(\phi, S_{p1}, S_{s1}, \lambda, \mu))$ is presented, which represents the equation of the adjoint state Plessix (2006). Where λ and μ, Lagrange multipliers, are called adjoint state variables, dual to the PP-PS travel times, where $d\Omega_1 = dxdz$:

$$\begin{aligned}\frac{\delta\mathcal{L}(\phi, S_{p1}, S_{s1}, \lambda, \mu)}{\epsilon} &= \int_\Gamma (\widetilde{T}^i_{ps}(T^i_{ps}(\phi, S_{p1}, S_{s1}) - T^{obs,i}_{ps}))ds + \int_\Gamma (\widetilde{T}^i_{pp}(T^i_{pp}(\phi, S_{p1}) - T^{obs,i}_{pp}))ds \\ &+ \int_{\Omega_1} \lambda \overbrace{(w_{ps} - \nabla\widetilde{T}_{ps}\nabla T_{ps}(\phi, S_{p1}, S_{s1}))}^{\text{From Eq. (17)}} d\Omega_1 \quad + \int_{\Omega_1} \mu \overbrace{(w_{pp} - \nabla\widetilde{T}_{pp}\nabla T_{pp}(\phi, S_{p1}))}^{\text{From Eq. (18)}} d\Omega_1. \\ &+ \mathcal{O}(\epsilon^2). \end{aligned} \tag{19}$$

4. Design of adjoint variables From the Variational Eikonal equations

Through consideration of the extended variational function, given by (19), in order to replace the $\widetilde{T}_{ps}$ and $\widetilde{T}_{pp}$ terms of the integrals defined over Γ, by adjoint variables, the constraint integrals set over Ω_1 are reformulated: $-\int_{\Omega_1}(\lambda\nabla\widetilde{T}_{ps}\nabla T_{ps}(\phi, S_{p1}, S_{s1}) + \mu\nabla\widetilde{T}_{pp}\nabla T_{pp}(\phi, S_{p1}))d\Omega_1$. This reformulation is accomplished using the first Green's identity, expressing them as a line integral (over Γ) and a surface integral (over Ω_1). The details of this process can be found in the Appendix B (Equations (54) and (55)). Thus, in the augmented variational approach, the line integrals over Γ can thus be related using the adjoint variables λ and μ, conditioned such that their definition substitutes for the integrals involving $\widetilde{T}_{ps}$ and $\widetilde{T}_{pp}$. In this context, the adjoint variables λ^i_Γ and μ^i_Γ must be tuned according to the specifications in Equations (20) and (23) (see Figure 5.a and 5.b). Furthermore, the divergences arising from the integrals defined over Ω_1 (see Appendix Equation (55)) are set to zero. Therefore, the adjoints $\lambda^i_{\Omega_1}$ and $\mu^i_{\Omega_1}$ are determined according to Equations (21) and (24) over the region Ω_1. Following the adjoint state formulation, Equation (19) (the geometric relationship of the adjoint variables can be seen in Figure 5.a and 5.b):

Figure 5

Backpropagation of the Adjoint Field at iteration k for shot$_i$: Conversion/Reflection adjoints are generated, first from boundary Γ downwards to $\phi = 0$, and next from $\phi = 0$ upwards.

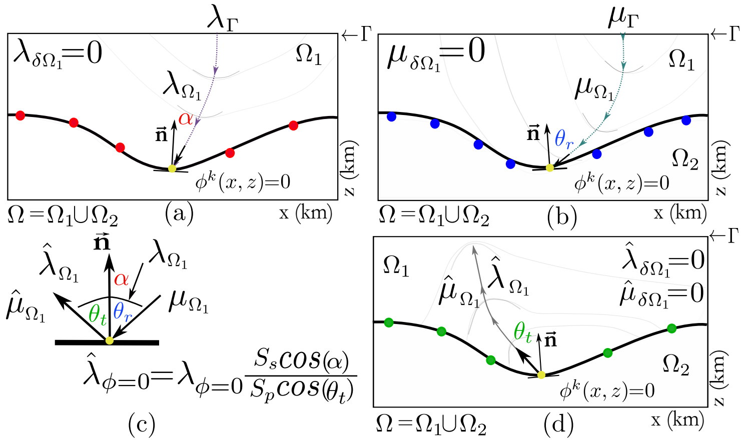

(a) Downward backpropagation of the adjoint of PS residual field. (b) Downward propagation of the adjoint of PP residual field. (c) Boundary condition on $\phi(x,z) = 0$ for the adjoints given by angle relationships determined by time gradients. (d) Upward propagation of the adjoints of PS and PP fields.

Adjoint design for converted PS field

$$\lambda_\Gamma^{k,i} \nabla T_{ps}^{k,i}(\phi^k, S_{p1}^k, S_{s1}^k) \cdot \ \mathbf{n} = T_{ps}^{k,i} - T_{ps}^{obs,i}, \ on \, \Gamma \tag{20}$$

$$-\nabla(\lambda_{\Omega_1}^{k,i} \nabla T_{ps}^{k,i}(\phi^k, S_{p1}^k, S_{s1}^k)) = 0, \ \ in \ \ \Omega_1^k \tag{21}$$

$$\lambda^{k,i} = 0, \ \ on \ \ \delta\Omega_1 \setminus \ R \cup \Gamma \tag{22}$$

Adjoint design for reflection PP field

$$\mu_{\Gamma}^{k,i}\nabla T_{pp}^{k,i}(\phi^k, S_{p1}^k)\cdot\mathbf{n} = T_{pp}^{k,i} - T_{pp}^{obs,i},\ \ on\ \ \Gamma \tag{23}$$

$$-\nabla(\mu_{\Omega_1^k}^{k,i}\nabla T_{pp}(\phi^k, S_{p1}^k)) = 0,\ \ in\ \ \Omega_1^k \tag{24}$$

$$\mu^{k,i} = 0,\ \ on\ \ \delta\Omega_1 \setminus R \cup \Gamma \tag{25}$$

Now, from the first Green's identity, the first variation in equation (19) can be rewritten in terms of integrals over Ω_1 and line integrals on the reflector R ($\delta\Omega_1(\phi = 0)$) as (see Figure 5.c and 5.d):

$$\frac{\delta\mathcal{L}}{\epsilon} = \int_{\Omega_1}(\lambda w_{ps})\ ds + \int_{\Omega_1}(\mu w_{pp})\ ds - \int_R \lambda\frac{\partial T_{ps}(\phi, S_{p1}, S_{s1})}{\partial n}\widetilde{T}_{ps}\, ds - \int_R \mu\frac{\partial T_{pp}(\phi, S_{p1})}{\partial n}\widetilde{T}_{pp}\, ds + \mathcal{O}(\epsilon^2)\ . \tag{26}$$

The terms $\int_R \lambda\tilde{T}_{ps}\nabla T_{ps}\cdot\mathbf{n}ds + \int_R \mu\tilde{T}_{pp}\nabla T_{pp}\cdot\mathbf{n}ds$ can be eliminated by using the transmitted propagation times T_{pt} from the source to the reflector. This allows the use of other adjoint operators, $\hat{\lambda}$ and $\hat{\mu}$, to cancel the integrals over the reflector R. This simplification is possible because the condition $T_{ps} = T_{pp} = T_{pt}$ is satisfied along the reflector, as shown in Figure 4.b, this condition leads to $\tilde{T}_{pt} = \tilde{T}_{ps} = \tilde{T}_{pp}$. The necessary considerations for eliminating $\tilde{T}_{pt}$ are derived from Green's first identity. These can be found in appendix equations (56) and (57). For the converted PS waves, $\hat{\lambda}$ must satisfy equations (27) to (29). Meanwhile, for reflected PP waves, $\hat{\mu}$ must satisfy equations (30) to (32).

$$\hat{\lambda}^i_{\phi=0}\frac{\partial T_{pt}}{\partial n} = -\lambda^i \frac{\partial T_{ps}}{\partial n}, \;\; on \;\; R \tag{27}$$

$$-\nabla(\hat{\lambda}^i_{\Omega_1}\nabla T_{pt}(\phi, S_{p1})) = 0, \;\; in \;\; \Omega_1 \tag{28}$$

$$\hat{\lambda}^i = 0, \;\; in \;\; \delta\Omega_1 \setminus R \tag{29}$$

$$\hat{\mu}^i_{\phi=0}\frac{\partial T_{pt}}{\partial n} = -\mu^i \frac{\partial T_{pp}}{\partial n}, \;\; on \;\; R \tag{30}$$

$$-\nabla(\hat{\mu}^i_{\Omega_1}\nabla T_{pt}(\phi, S_{p1})) = 0, \;\; in \;\; \Omega_1 \tag{31}$$

$$\hat{\mu}^i = 0, \;\; in \;\; \delta\Omega_1 \setminus R \tag{32}$$

The computation of adjoints $\hat{\lambda}^i_{\phi=0}$ and $\hat{\mu}^i_{\phi=0}$ on the reflector R is performed by equations (27) and (30), where the angles of the gradient vectors $\nabla T_{pt}(\phi, S_{p1})$, $\nabla T_{pp}(\phi, S_{p1})$ and $\nabla T_{ps}(\phi, S_{p1}, S_{s1})$ with respect to the normal vector of the interface curve $\phi = 0$ are used (see Figure 5.c, Figure 4, and Figure 17 in Appendix C). With these angular relations established and the values of λ and μ already known, it is possible to calculate the adjoint $\hat{\lambda}$ for the PS field along the reflector R:

$$\hat{\lambda}^i_{\phi=0}\frac{\partial T_{pt}}{\partial n} = -\lambda^i_{\phi=0}\frac{\partial T_{ps}}{\partial n}, \ \ on \ \ R,$$

$$\hat{\lambda}^i_{\phi=0}\nabla T_{pt}\cdot\mathbf{n} = -\lambda^i_{\phi=0}\nabla T_{ps}\cdot\mathbf{n}, \ \ on \ \ R,$$

$$\hat{\lambda}^i_{\phi=0}|\nabla T_{pt}||n|cos(\theta_t) = -\lambda^i_{\phi=0}|\nabla T_{ps}||n|cos(\pi-\alpha), onR,$$

$$\hat{\lambda}^i_{\phi=0}\, S_p\, cos(\theta_t) = \lambda^i_{\phi=0}\, S_s\, cos(\alpha), \qquad on \ \ R,$$

The relationship between λ and $\hat{\lambda}$ is determined by the Snell law, see Figure 5.c:

$$\hat{\lambda}^i_{\phi=0} = \lambda^i_{\phi=0}\frac{S_s\, cos(\alpha)}{S_p\, cos(\theta_t)}, \quad on \ \ R. \tag{33}$$

Similarly, given these angular relationships for the reflection PP field, the adjoint $\hat{\mu}$ is calculated from μ as:

$$\hat{\mu}^i_{\phi=0}\frac{\partial T_{pt}}{\partial n} = -\mu^i\frac{\partial T_{pp}}{\partial n}, \ \ on \ \ R$$

$$\hat{\mu}^i_{\phi=0}\nabla T_{pt}\cdot\mathbf{n} = -\mu^i\nabla T_{pp}\cdot\mathbf{n}, \quad on \ \ R$$

$$\hat{\mu}^i_{\phi=0}\, S_p\, cos(\theta_t) = -\mu^i\, S_p\, cos(\pi-\theta_r), \quad on \ R$$

The Snell law ratio between $\hat{\mu}$ and μ considers the same propagation medium S_p; therefore, $\theta t = \theta r$ and $\hat{\mu} = \mu$. This result is similar to that obtained for P-waves acquired with

Crosswell geometry in Li et al. (2014).

$$\hat{\mu}^{i}_{\phi=0} = \mu^{i} \ on \ \ R \tag{34}$$

The adjoint equations correspond to PDE that are solved by backpropagation, starting from the values at the boundary Γ (Figure 5) over the entire Ω_1 region. The remaining adjoints at the reflector R ($\hat{\mu}^{i}_{\phi=0}$ and $\hat{\lambda}^{i}_{\phi=0}$) are propagated upwards through Ω_1 to the Γ boundary on the surface, as indicated in Figure 5.d. The use of the designed adjoints (λ, μ, $\hat{\mu}$ and $\hat{\lambda}$) allow the development of a PP-PS tomography where solving the inversion problem requires the same computational cost of a forward problem. So, having established the adjoints, these can feed into the second part of the Lagrangian, Equation 19 related to the w_{ps} and w_{pp} to determine the perturbations $\widetilde{\phi}(x,z)$, $\widetilde{S}_{p1}(x,z)$ and $\widetilde{S}_{s1}(x,z)$ which update the parameters ϕ, S_{p1} and S_{s1} such that the time residuals are minimised, Equations 6. Equation 19 results in an integral over Ω_1 in terms of the adjoints (lagrange multipliers) acting on w_{pp} , w_{ps} and w_{pt} as:

$$\frac{\delta \mathcal{L}}{\epsilon} = \int_{\Omega_1} (\lambda w_{ps} + \mu w_{pp}) d\Omega_1 + \int_{\Omega_1} (\hat{\lambda} + \hat{\mu}) w_{pt} d\Omega_1. \tag{35}$$

The quantities w_{pp} and w_{ps} are independent of travel times and are determined by the model variables and their perturbations $\widetilde{\phi}$, $\widetilde{S}_{p1}$ and $\widetilde{S}_{s1}$. Since $w_{pt} = w_{pp}$ the equation (35) can be regrouped in terms of the update perturbations:

$$\frac{\delta \mathcal{L}}{\epsilon} = \int_{\Omega_1} (\lambda A_s + (\mu + \hat{\mu} + \hat{\lambda}) A_p) \nu \widetilde{\phi}\, d\Omega_1 + \int_{\Omega_1} \lambda B_s \widetilde{S}_{s1}\, d\Omega_1 + \int_{\Omega_1} ((\mu + \hat{\mu} + \hat{\lambda}) B_p) \widetilde{S}_{p1}\, d\Omega_1 + \mathcal{O}(\epsilon^2) \leq 0 \tag{36}$$

For the minimization of $\frac{\delta E}{\epsilon} \leq 0$, (37) to (39) are obtained to compute perturbations $\tilde{\phi}(x,z)$, $\tilde{S}_{s1}(x,z)$, and $\tilde{S}_{p1}(x,z)$ such that they update $\phi(x,z)$, $S_{s1}(x,z)$, and $S_{p1}(x,z)$ in a descent direction considering all shots, as follows:

$$\tilde{\phi}^k(x,z) = -\sum_{i=1}^{N=49} (\lambda^{k,i} A_s^k + (\mu^{k,i} + \hat{\lambda}^{k,i} + \hat{\mu}^{k,i}) A_p^k) \tag{37}$$

$$\tilde{S}_{s1}^k(x,z) = -\sum_{i=1}^{N=49} (\lambda^{k,i}) B_s^k \tag{38}$$

$$\tilde{S}_{p1}^k(x,z) = -\sum_{i=1}^{N=49} (\mu^{k,i} + \hat{\lambda}^{k,i} + \hat{\mu}^{k,i}) B_p^k \tag{39}$$

5. Numerical implementation

This section presents the numerical implementation of the proposed PS-PP tomography algorithm. In the first iteration, the initial position of the reflector geometry model, represented by $\phi^{k=0}(x,z)=0$, is defined and the region $\Omega_1^{k=0}$ ($\phi^{k=0}(x,z)<0$) is established. Here the initial slowness models $S_s^{k=0}(x,z)$ and $S_{p(x,z)}^{k=0}$ are assigned as well. Using the methodology described in section 3.1, the travel times $T_{ps}(\phi^{k=0}, S_s^{k=0}, S_p^{k=0})$ and $T_{pp}(\phi^{k=0}, S_p^{k=0})$ are calculated and compared with the observed T_{ps}^{obs} and T_{pp}^{obs} for each shot $_i$.

The algorithm is implemented to model the first layer, which is defined by Ω_1; therefore, head waves and refractions are not included in the reflection-conversion (PP-PS) tomographic solution. The transmitted, reflection and conversion times in Ω_1 are calculated using the Multistencils FMM according to Hassouna and Farag (2007). This approach, following the method described in Kroon (2009), is adapted to calculate travel times from $Shot_i$ position to each point on the curve $\phi(x,z)=0$, where the reflection-conversion takes place. From the travel times determined at these points, the FMM method is used to calculate the PS conversion and PP reflection times, which propagate upwards until they reach the surface Γ, as shown in Figure 4.

As we show in the previous section, the calculation of the adjoint fields is fundamental for the solution of the inverse problem. It involves the backpropagation of the PS-PP residual time fields: $(T_{ps}^i(\phi, S_{p1}, S_{s1}) - T_{ps}^{obs,i})$ and $(T_{pp}^i(\phi, S_{p1}) - T_{pp}^{obs,i})$. As shown in Figure

5, the backpropagation is performed from the free surface Γ to the reflector ($\phi(x,z) = 0$). The adjoint fields (λ, μ, $\hat{\lambda}$ and $\hat{\mu}$) are expected to tend to zero as the residual times are minimised. The necessary algorithms to compute perturbations: $\tilde{\phi}(x,z)$, $\tilde{S}_p(x,z)$, and $\tilde{S}_s(x,z)$ are described in the following sections using the FSM methodology presented in Taillandier et al. (2009). Additionally, heuristics for weighting factors are proposed to ensure stable convergence of model updates for $\phi(x,z)$, $S_p(x,z)$, and $S_s(x,z)$ towards the true model.

5.1. 2D Sampling

Given that the aim is to evaluate the performance of the developed algorithm on synthetic data in different scenarios of V_s and V_p, with geometries defined by $\phi = 0$, it is appropriate to discretise the space Ω with a grid that maintains a realistic distance between nodes while minimising their number to maintain computational efficiency. Grids with dimensions between 50×50 and 200×200 are used to model a 2D region Ω of 2×2 km, such that $dx = dz = 0.0408 - 0.010$ km, where dx and dz represent the horizontal and depth spatial resolution respectively. In this range, velocities between [1, 1.25] km/s for P-waves and [0.33, 0.75] km/s for S-waves are considered. The spatial sampling is set to balance CPU processing time with compliance with the CFL condition, which ensures numerical stability if it is satisfied between each iteration that $\Delta t \leq \frac{\Delta x}{C}$[2]. The CPU on which the FMM method is applied must be able to satisfy this condition to ensure that the travel time calculations are correctly sampled over each grid point. Thus, a mesh that meets the requirements of mini-

---

[2] $C = \frac{v_{average}}{v_{max}} = \frac{0.77}{1.25} = 0.66\frac{km}{s}$

Figure 6

Representation of the 2 km spatial model on a grid of 79×79 cells.

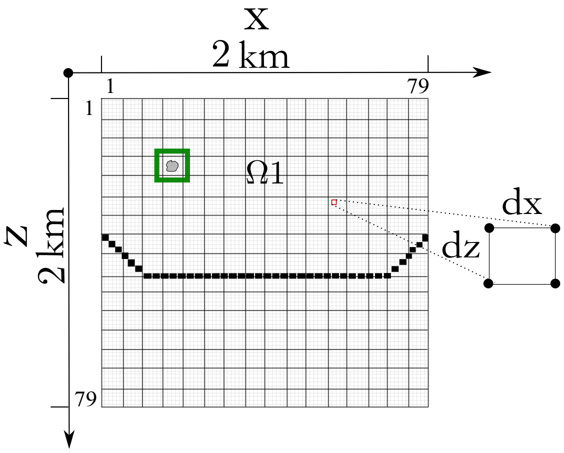

Black cells represent the position of reflector $\phi(x, z) = 0$. Maximum spatial resolution display corresponds to the green box in the grid.

mum sampling, numerical stability (CFL) and distance between grid points that simulates reality is: 79 × 79 cells defined by $dx = dz = 0.0256$ km. See Figure 6.

5.2. Calculation of travel times for PP and PS fields.

The proposed tomography methodology focuses on the numerical definition of a conversion-reflection surface. This surface is used to calculate the travel times of PS and PP waves. Once the grid defining the space Ω is established, a numerical solution strategy for the eikonal equation over Ω_1 is implemented. This space is defined by either V_p or V_s depending on the case. The RS-FMM methodology, as described in 3.1, is used for this. This procedure is conditional on the definition of the coordinates (x, z) within the reflector model defined by $\phi(x, z) = 0$. These coordinates are determined by searching for a change of sign within the function $\phi(x, z)$, within a limited distance of $|3 \cdot dx|$, as indicated in Li et al. (2014). This approach aims to optimise the exploration process.

The calculation of travel times is performed using the software developed in Kroon (2009). This software follows the methodology described in Hassouna and Farag (2007) and was originally designed for a single source. However, it is adapted to compute $T^i_{pp}(\phi, S_{p1})$ (equation (4)) and $T^i_{ps}(\phi, S_{p1}, S_{s1})$ (equation (5)) as these come from multiple positions, especially where $\phi(x, z) = 0$. This adaptation treats these calculations as though they result from multiple sources being triggered simultaneously.

5.2.1. Calculation of the observed times T^{obs}_{ps} and T^{obs}_{pp} from true velocities and reflector geometry

In our synthetic numerical experiments, we simulate real field measurements by using true velocity models to calculate the observed times typically recorded in real field experiments. The true models, for a spatial domain Ω, are divided by a continuous (or piecewise continuous) curve representing the true reflector delineating the first subsurface layer Ω_1. Because we invert the first reflector, it could represent either the bottom of the weathering later (Near-surface) layer or a shallow (bedrock) reflector, both of which indicate a discontinuity between two velocity fields. A 3C multicomponent seismic acquisition (explosive source - 3C receivers) is numerically simulated for 49 sources sequentially activated to illuminate Ω_1.

We simulate four representative geometries of real geological reflectors: syncline, sinusoid, monocline and step discontinuity. These curves, modelled by the mathematical equations described in section 6 and located at an average depth of about 700 m, are defined along with the true velocity fields $V_s(x, z)$ and $V_p(x, z)$ for the first layer Ω_1. The algorithm that solves the forward problem for each $shot_i$ is then executed, resulting in the travel times of the first arrivals on the free surface Γ: $T_{ps}^{obs,i}$ and $T_{pp}^{obs,i}$ (see section 3.1). A representation of these observed times is given in Figure 1-a. The corresponding spatial model for a given shot is shown in Figure 1-b. In real field data, the observed times are measured by selecting hyperbolic events in shot gathers for both PS and PP wave modes, typically in the radial and vertical components, respectively.

5.3. Adjoint equation: Inversion

Analogous to the forward model, where the zero level of the contour evolves according to the equation $\phi_t + v|\nabla\phi| = 0$, where $|\nabla\phi|$ represents the gradient of the update, in the inverse model, adjoint operators are used to estimate the correct evolution of the zero contour in the inversion of the level set function ($\tilde{\phi}(x,z)$, $\tilde{S}_{s1}(x,z)$, and $\tilde{S}_{p1}(x,z)$). The parameter v serves as a stability factor in the contour evolution.

The adjoint variables developed in section 4 are used for seismic inversion. Initially, the adjoints at the Γ boundary are determined by the relationship between the time residuals and the gradient of the PS-PP arrival times. These relationships are expressed as $\mu_\Gamma = \frac{(T_{pp}(\phi,S_{p1})-T_{pp}^{obs})}{\frac{\partial T_{pp}}{\partial z}|\Gamma}$ and $\lambda_\Gamma = \frac{(T_{ps}(\phi,S_{p1},S_{s1})-T_{ps}^{obs})}{\frac{\partial T_{ps}}{\partial z}|\Gamma}$, and they are defined by the equations (20) and (23). The geometric relationship of these variables is shown graphically in figures 5.a.b.

The adjoint fields are then backpropagated through Ω_1 space, taking into account the time gradients computed at each grid point using the forward problem solution presented in section [3]. Once the adjoints at the μ_Γ and λ_Γ boundary are established, along with the PS-PP travel times within Ω_1 for transmissions T_{pt}, converted T_{ps} and reflections T_{pp}, the gradients ∇T_{pt}, ∇T_{pp} and ∇T_{ps} can be calculated. This allows us to define the adjoints of the PS-PP body waves using the equations (21) and (24). The spatial relationship of these variables is shown in the diagram of figure 5.a.b.

The computation of the adjoint fields μ_{Ω_1} and λ_{Ω_1}, analogous to the direct problem, is performed by backpropagating the adjoint fields μ_Γ and λ_Γ from the boundary Γ over the time fields T_{ps}, T_{pp} and T_{pt} defined in Ω_1 by solving the equations (21) and (24). This methodology follows the "fast sweep" strategy. The algorithm requires several iterations to converge, unlike the FM method used in the direct solution, which converges in a single iteration. For the PS field, the partial differential equation $\frac{\partial}{\partial x}(\frac{\partial T_{ps}}{\partial z}\lambda_{\Omega_1}) + \frac{\partial}{\partial z}(\frac{\partial T_{ps}}{\partial z}\lambda_{\Omega_1}) = 0$ (equation (21)) is solved using a forward finite difference scheme. The adjoint μ_{Ω_1} is calculated in a similar way. Numerical details are described in Leung and Qian (2006) and Taillandier et al. (2009), and the algorithms developed are presented in Daniel (2019).

Finally, to satisfy the equation (19), the adjoints μ and λ are conditioned on the lateral boundaries. Here the equations (22) and (25) must be satisfied in $\delta\Omega_1$: $\mu_{\delta\Omega_1} = 0$ and $\lambda_{\delta\Omega_1} = 0$, as shown in the scheme of figure 5.a.b.

5.3.1. *Solution of adjoint $\hat{\lambda}$ on reflector boundary $\phi(x,z) = 0$*

On the reflector $\phi(x,z) = 0$ the adjoint fields μ and λ have a boundary condition to be solved, from the equation(26), thus that the time variations on the reflector are canceled, $\int_{R:\phi(x,z)=0} \lambda \tilde{T}_{ps} \nabla T_{ps} \cdot \mathbf{n}\, ds + \int_{R:\phi(x,z)=0} \lambda \tilde{T}_{pp} \nabla T_{pp} \cdot \mathbf{n}\, ds$.

Applying the first green identity again, we obtain new adjoints $\hat{\lambda}$ and $\hat{\mu}$ which eliminate $\tilde{T}_{ps}$ over the reflector. The algebraic development leads to the equations (33) and (34).

As previously mentioned, the coordinates of the reflector $\phi(x,z)=0$ are determined by identifying the sign changes of the function $\phi(x,z)$ on the grid used to discretise the studied space. At each of these coordinates, $\hat{\mu}$ is equal to μ for the PP field. For the PS field, the adjoint $\hat{\lambda}$ is governed by Snell's law for an elastic medium, as shown in equations (33) and (34). In the latter field, each reflector coordinate must satisfy $\hat{\lambda}=\lambda\frac{S_s\cos(\alpha)}{S_p\cos(\theta_t)}$, which implies the need to calculate the conversion angle α and the arrival angle θ_t. These angles are measured by calculating the gradients ∇T_{pt} and ∇T_{ps} near the interface $\phi(x,z)=0$, as shown in figures 4 and 5. Measuring these angles also involves determining the coordinates of the normal vector to the surface $\phi(x,z)=0$, calculated as $\mathbf{n}=\frac{\nabla(\phi(x,z)=0)}{|\nabla(\phi(x,z)=0)|}$.

The adjoint equations are solved upwards within the medium Ω_1, towards the surface Γ, once the adjoints $\hat{\mu}$ and $\hat{\lambda}$ have been computed at the reflector $\phi(x,z)=0$. The equations (31) and (28) are used, taking into account the field T_{pt}. The numerical solution follows the procedure described above for the calculation of μ_{Ω_1} and λ_{Ω_1}. Finally, the lateral boundary conditions $\hat{\mu}_{\delta\Omega_1}=0$ and $\hat{\lambda}_{\delta\Omega_1}=0$ of the equations (29) and (32) are satisfied. Figure 5 a. b shows the spatial interaction of these equations.

The perturbations $\tilde{\phi}(x,z)$, $\tilde{S}_{s1}(x,z)$, and $\tilde{S}_{p1}(x,z)$ are obtained by summing all the calculated adjoints for the N shots, as indicated in equations (37) to (39).

5.4. Regularization of perturbations ($\tilde{\phi}(x,z)$, $\tilde{S}_s(x,z)$ and $\tilde{S}_p(x,z)$) and filtering of slownesses ($S_s(x,z)$ and $S_p(x,z)$)

The mathematical modelling of the inversion for both the direct (time) and inverse (adjoint) problems requires the solution of partial differential equations (PDEs). Errors in the solutions propagate throughout Ω_1 space due to numerical discretisation, boundary geometry, normal vector approximation and illumination of Ω_1 determined by the acquisition geometry. These discrepancies are incorporated by the adjoint gradient fields which update $\phi(x,z)$, $S_{s1}(x,z)$ and $S_{p1}(x,z)$. A regularisation of the updating perturbations $\tilde{\phi}(x,z)$, $\tilde{S}_{s1}(x,z)$ and $\tilde{S}_{p1}(x,z)$ is performed to ensure stability and convergence to the true model in tomography.

To eliminate the abrupt variation components of $\tilde{S}_{s1}(x,z)$, we use a Laplacian regulariser defined by the differential equation for the PS field: $(I-\kappa(\frac{\partial^2}{\partial x^2}+\frac{\partial^2}{\partial z^2}))\tilde{S}_s(x,z) = \lambda(x,z)\cdot B_s(x,z)$; looking for a solution where the inverse problem is well-posed. The implementation of this regulariser is done in the frequency domain, as shown below:

$$\begin{aligned}
\tilde{S}_s(W_x,W_z) =& \frac{1}{1+\kappa[W_x^2+W_z^2]}(\lambda)B_s(W_x,W_z) \\
\tilde{S}_p(W_x,W_z) =& \frac{1}{1+\kappa[W_x^2+W_z^2]}(\mu+\hat{\lambda}+\hat{\mu})B_p(W_x,W_z),
\end{aligned}$$

where $(W_x,W_z)\in[-\pi,\pi]$ in 2D. We used $\kappa=1$ for smoothing without removing important information from the adjoints.

Also, to better delineate the different contour levels in the $\phi(x,z)$ function, so that the reflector at $\phi(x,z)=0$ is reliably located, a discrete Laplacian and a curvature factor are used, as defined in:

$$\phi(x,z)^{regDist} = \underbrace{((\frac{\partial^2\tilde{\phi}(x,z)}{\partial x^2}+\frac{\partial^2\tilde{\phi}(x,z)}{\partial z^2}))}_{DiscreteLaplacian} - \overbrace{\nabla(\frac{\nabla(\tilde{\phi}_{(x,z)})}{|\nabla(\tilde{\phi}_{(x,z)})|})}^{Curvature}.$$

Thus, $\tilde{\phi}(x,z)$ coming from the sum of adjoints, equation (37), is recalculated as $\tilde{\phi}(x,z) = \tilde{\phi}(x,z) + \gamma\phi^{regDist}(x,z)$; being the optimal γ for the PS-PP tomography found as 0.01, Li et al. (2010) and Osher and Fedkiw (2005).

In PS-PP tomography, the shape of the reflector $\phi(x,z) = 0$ influences the spatial distribution of the fields S_P and S_S. To mitigate this effect during the inversion process, the results presented in Wang et al. (2022) are applied, which suggest a direct and subtle smoothing of the solution models S_s and S_p at each iteration. These authors recommend applying a subtle smoothing directly to the solution models S_s and S_p during the inversion process in order to counteract the variability induced on these fields by the shape of the reflector $\phi(x,z) = 0$ at each iteration of the developed PS-PP tomography. A Laplacian filter is implemented in a similar way to the one used to regularise $\tilde{\phi}(x,z)$ and $\tilde{S}_s(x,z)$. In this procedure, the coefficient α is significantly reduced, reaching exactly 0.3. This ensures a mild smoothing effect.

5.5. Update process

Finally, with the computed perturbations $\tilde{\phi}(x,z)$, $\tilde{S}_{s1}(x,z)$, and $\tilde{S}_{p1}(x,z)$, the reflector and slowness models are updated as:

$$\phi^k(x,z) = \phi^{k-1}(x,z) + \mathit{\Psi}\epsilon\nu\tilde{\phi}(x,z), \tag{40}$$

$$S_p^k(x,z) = S_p^{k-1}(x,z) + \eta\epsilon\tilde{S}_p(x,z), \tag{41}$$

$$S_s^k(x,z) = S_s^{k-1}(x,z) + \zeta\epsilon\tilde{S}_s(x,z), \tag{42}$$

The fitting parameters ϵ and ν are defined as $\epsilon = 1e^{-3}$ and $\nu = 1e^{-3}$ respectively, following the recommendations given in Leung and Qian (2006) and Li et al. (2014). In addition, the additional parameters Ψ, η and ζ are determined heuristically, and their choice is supported by experimental tests mentioned in section 6. The aim of this parameter configuration is to achieve a balance in convergence between stability and number of iterations.

In the experiment presented in section 6.1, only $\phi(x, z)$ is inverted, while the true values of $S_p(x, z)$ and $S_s(x, z)$ are kept fixed. This choice allows the level $\phi(x, z) = 0$ to converge to the true reflector and sets $\mathit{\Psi}$ to 1.25. In the experiment described in section 6.2, the inversion of $\phi(x, z)$ and $S_s(x, z)$ is performed simultaneously, taking into account the true value of $S_p(x, z)$. In this case ζ is set to 0.125. Finally, in the experiment described in section 6.3, both $\phi(x, z)$ and $S_p(x, z)$ are inverted simultaneously, taking into account the true value of $S_s(x, z)$. For this configuration η is set to 0.025. The strategy starts with the sets $\mathit{\Psi} = 1.25$, $\zeta = 0.125$ and $\eta = 0.025$, which are multiplied by a factor of 2 every 10,000 iterations until convergence is reached, when $\phi(x, z)$, $S_p(x, z)$ and $S_s(x, z)$ are inverted simultaneously..

5.6. Re-initialization of distance funciton $\phi^k(x, z)$

Distance-to-reflector contours described by function $\phi(x, z)$ are degraded when updated in each iteration with perturbation $\tilde{\phi}(x, z)$, as in Equation (40). This phenomenon makes difficult to define the contour of the zero level ($\phi(x, z) = 0$) with precision. This progressive degradation becomes particularly evident when the proposed tomography algorithm is iterated.

The process of **re-initialization** aims, without modifying the localization of $\phi(x,z) = 0$, to redefine the distances to the zero level trying to maintain for all Ω the condition that $|\nabla\phi(x,z)| = 1$. Osher and Fedkiw (2005) recommend the use of Godunov's methodology for the calculation of the gradient of $\phi(x,z)$ and propose to redefine the distance function $\phi(x,z)$ using the equation following:

$$\frac{\partial\phi(x,z)}{\partial T} = \frac{\phi^{\text{Reinitialize}}(x,z) - \phi(x,z)}{\Delta T} \quad = S_{\text{even}}(\phi(x,z))(1 - |\nabla\phi(x,z)|).$$

$$\phi^{\text{Reinitialize}}(x,z) = \phi(x,z) + \Delta T S_{\text{even}}(\phi(x,z))(1 - |\nabla\phi(x,z)|),$$

where ΔT is the sampling step size used to track the internal motion of $\phi(x,z) = 0$ during the regularization process (in this paper $\Delta T = 0.0128$), and $S_{even}(\phi(x,z)) = \frac{\phi(x,z)}{\sqrt{(\phi(x,z))^2 + min(dx,dz)^2}}$. The development of the proposed PS converted-wave tomography methodology performs the re-initialization using the implementation developed by Pelissier (2023), where, in addition, within the iterative process of approximating $|\nabla\phi(x,z)| = 1$, it defines an optimal ΔT for the update of $(\phi^k(x,z))^{\text{Reinitialize}}$.

5.7. Algorithm

An overview of the algorithm used to implement the proposed **Tomo_PP-PS** tomography is presented here:

Inputs: $T_{ps}^{obs,1:N=49}$ $T_{pp}^{obs,1:N=49}$

$[\boldsymbol{\phi}, \boldsymbol{V_s}, \boldsymbol{V_p}]$ ←**Tomo_PP-PS($\boldsymbol{\phi^{k=0}}$, $\boldsymbol{V_s^{k=0}}$, $\boldsymbol{V_p^{k=0}}$)**

```
≫ while (Condition ==1) [3]
≫   $P_R(x_R, z_R) \leftarrow \phi^k(x,z) = 0$: $ReflectorPosicion$
≫   $S_s^k(x,z) = S_{s2}^k(x,z)H_\tau(\phi^k) + S_{s1}^k(x,z)(1 - H_\tau(\phi^k))$
≫   $S_p^k(x,z) = S_{p2}^k(x,z)H_\tau(\phi^k) + S_{p1}^k(x,z)(1 - H_\tau(\phi^k))$
≫   Compute: $A_p^k(x,z)$; $A_s^k(x,z)$; $B_s^k(x,z)$; $B_p^k(x,z)$
≫     for $\mathbf{i = 1 : N} \rightarrow Shot_i$
            Forward Problem
≫       RS-FMM:$T_{pp}^{k,i}(\phi, S_{p1})$, $T_{ps}^{k,i}(\phi, S_{p1}, S_{s1})$
≫       $\boldsymbol{R}_{pp} = T_{pp}^{k,i}(\phi, S_{p1}) - T_{pp}^{obs,i}$
≫       $\boldsymbol{R}_{ps} = T_{ps}^{k,i}(\phi, S_{p1}, S_{s1}) - T_{ps}^{obs,i}$
            Inverse Problem
≫       Fastsweeping : $\lambda^i \leftarrow \boldsymbol{R}_{ps}$   $\mu^i \leftarrow \boldsymbol{R}_{pp}$
≫         $\hat{\lambda}^i_{\phi=0} = \lambda^i_{\Omega_1}(\frac{S_s(x,z)cos(\alpha)}{S_p(x,z)cos(\theta_t)})$ , $\hat{\mu}^i_{\phi=0} = \mu^i$
≫     endfor
≫   $\lambda = \sum_{i=1}^N \lambda^i$  $\mu = \sum_{i=1}^N \mu^i$  $\hat{\lambda} = \sum_{i=1}^N \hat{\lambda}^i$  $\hat{\mu} = \sum_{i=1}^N \hat{\mu}^i$
≫   $\tilde{\phi}^k(x,z) = -\lambda A_s + (\mu + \hat{\lambda} + \hat{\mu})A_p + (\phi^k(x,z))^{regDist}$
≫   $\tilde{S}_{s1}^k(x,z) = Regularization(-\lambda B_s)$
≫   $\tilde{S}_{p1}^k(x,z) = Regularization(-(\mu + \hat{\lambda} + \hat{\mu})B_p)$
≫   $\phi^{k+1}(x,z) = \phi^k(x,z) + \Psi\epsilon\nu\tilde{\phi}^k(x,z)$
≫   $S_{p1}^{k+1}(x,z) = S_{p1}^k(x,z) + \eta\epsilon\tilde{S}_{p1}^k(x,z)$
≫   $S_{s1}^{k+1}(x,z) = S_{s1}^k(x,z) + \zeta\epsilon\tilde{S}_{s1}^k(x,z)$
≫   $\phi^{k+1}(x,z) = (\phi^{k+1}(x,z))^{\text{Reinitialize}}$
≫   $[S_{p1}^{k+1}(x,z), S_{s1}^{k+1}(x,z)] \overset{\text{Smoothing\_filter}}{=} (S_{p1}^{k+1}(x,z), S_{s1}^{k+1}(x,z))$
≫ endwhile
```

Output:

$[\boldsymbol{\phi}^{k=end}(x,z), S_s^{k=end}(x,z), S_p^{k=end}(x,z)]$

---

[3] Stopping criterion: by the maximum number of iterations $((\#iter_{max}))$ or by the energy function E being less than $0.3 * dx$, where dx is the spatial resolution of the solution mesh Li and Leung (2013), as described with: $(\#\mathbf{iter_{max}}) \vee (E(\phi, S_{p1}, S_{s1}) < 0.3 * (dx))$.

6. Numerical Tests

In this section we present 2D numerical tests for validating the ideas presented theoretical framework and the evaluation of the performance of the developed PS-PP converted wave tomography algorithm. These tests are based on the estimation of the parameters: $[\boldsymbol{\phi}, \boldsymbol{V_s}, \boldsymbol{V_p}] \leftarrow$**Tomo_PS-PP**$(\boldsymbol{\phi^{k=0}},\ \boldsymbol{V_s^{k=0}},\ \boldsymbol{V_p^{k=0}})$,under four different true model geometrical and geological configurations defined on the basis of the geometry of the so-called true reflector and the velocity fields. Each model has a different reflector geometry which defines the geometry of the region Ω_1 and where V_s and V_p are assigned. The reflector geometries are defined in Table 1.

For the first group of tests we consider homogeneous true velocities on Ω_1: $V_s = 0.5$km/s and $V_p = 1$km/s. The second group of tests is defined by adding a velocity intrusion to the homogeneous models. The velocity intrusion follows the equation:

$$0.25e^{\frac{-(z-\Delta_z)^2}{\varnothing_z^2} - \frac{-(x-\Delta_x)^2}{\varnothing_x^2}}, \tag{43}$$

Table 1
The reflector geometries.

Model	Equation
Synclinal	$z_1(x) = 2.5 - 0.25 \cdot \sqrt{1.5^2 - (x-1)^2}$
Monocline	$z_2(x) = -0.35x + 0.97$
Sinusoidal:	$z_3(x) = 0.65 - 0.25\sin(\pi x)$
Discontinuous step:	$z_4(x) = 0.6\ if\, 0 \leq x < 0.875\ \ \&\ \ 1.2\ \ if\, 0.875 < x \leq 2.\ x = 0.875$km

Figure 7

Circular Gaussian velocity anomaly,

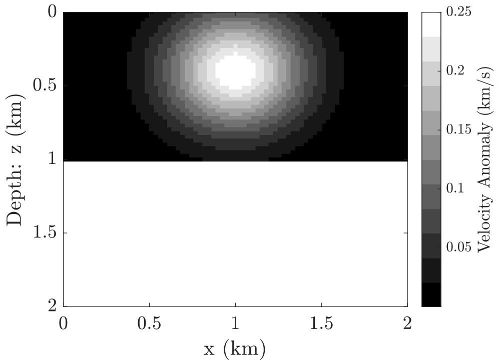

of parameters $\varnothing_z = \varnothing_x = 0.4km$ *and* $\Delta_z = 0.4km$ $\Delta_x = 1km$.

where Ø is the diameter and $\Delta_{x,z}$ is the center of the anomaly in km, see Figure 7. Once the velocity models are built, observed timess T^{obs}_{ps} and T^{obs}_{pp} are calculated for each simulation as described in the introduction to Section 3.

With the definition of this initial model for iteration $k = 0$, the developed tomography inversion process starts. The initial reflector geometry corresponds to a flat line located at 20 m from surface Γ, i. e. $\phi^{k=0}(x, 0.02) = 0$. This defines the initial region $\Omega_1^{k=0}$, where homogeneous velocities are initially defined as $V_s^{k=0} = 0.25$ km/s and $V_p^{k=0} = 0.5$ km/s.

6.1. Test 1: Inversion of reflector $\phi(x, z) = 0$ when true V_s and V_p are known

In this first set of tests, considering homogeneous true models, $V^{true} = 0.5$ km/s and $V^{true} = 1$km/s are known, in the region $\Omega_1^{k=0}$ defined by the initial reflector model $\phi^{k=0}(x, z)$. This initial configuration is identified in the upper left frame for each model panel as shown in Figure 8. Using the initial model ($k = 0$) we calculate $T_{ps}(\phi, S_{p1}, S_{s1})$ and $T_{pp}(\phi, S_{p1})$ as described in section 3.1 and compare them with the observed times. The evolution of the reflector ($\phi^{k=0,\ldots,end}(x,z)$) is shown in the subsequent rows of each model pannel in Figure 8 for sampled iterations. This first test is carried out to verify the effectiveness of the design of the adjoint variables in adequately solving the perturbation $\tilde{\phi}(x,z)$ in equation (37) checking that numerical instabilities do not affect the updating of function $\phi(x,z)$. If succesful, the initial flat reflector evolves in each iteration converging to the position and geometry of the true reflector (Figure 8).

The positional differences between the true reflector and the reflector geometry at k^{th} iteration, $\phi^k(x,z)=0$, are assessed computing the mean absolute position error, $\mathrm{MAPE}^k_{\phi=0}$ [4] (see first column in Figures 8-(a) to 8-(d)). Very small errors, between 0.3 % to 1.4 %, are obtained in the last iteration for all reflector geometries. Second and third columns in Figures 8-(a) to 8-(d) also present how the average of $T_{ps}(\phi, S_{p1}, S_{s1})$ (blue line) for the 49 shots, as well as the average of $T_{pp}(\phi, Sp1)$ (green line), measured for the models V_s^k and V_p^k obtained by the inversion process, converge to the observed travel times (black dashed lines) T_{ps}^{obs} and T_{pp}^{obs}. Table 2 shows the behaviour of the absolute relative errors between the observed and measured times. It is important to note that for the reflector with a discontinuity (Pannel 8-(d)) the inverted reflector $\phi(x,z)=0$ does not reproduce the discontinuity. However, it have a good convergence in the flat parts.

---

[4] For the total number of grid points on the true reflector, $\#Pts_R = 69$, the mean absolute percentage error between true reflector positions (Pts_R) and the inverted ones (ϕ_0) corresponds to: $\mathrm{MAPE}_{\phi=0} = \frac{1}{\#Pts_R}\sum_{i=0}^{\#Pts_R} |\frac{\phi_0 - Pts_R}{Pts_R}| \cdot 100$ %

Table 2

*Inversion of reflector in homogeneous medium with known V_s and V_p: [$\boldsymbol{\phi}$] ←**Tomo_PS-PP($\phi^{k=0}$,V_s,V_p)**. For each measured variable, the minimum (in grey) and maximum (bold) values are highlighted.*

Reflector Geometry	MAPE$_{\phi=0}$ (%)	R.errTps (%)	R.errTpp (%)	# of Iteration
Syncline	0.29	0.26	0.03	1900
Monocline	***1.36***	***0.64***	***0.27***	8600
Sine	0.7	0.14	0.1	***9400***
Discontinuous	0.83	0.02	0.1	1700

The last row of Figures 8-(a) to 8-(d) shows the spatial distribution of the relative error between the average for all shots of times $T_{ps}(\phi, S_{p1}, S_{s1})$ and $T_{pp}(\phi, S_{p1})$ and the observed times T_{ps}^{obs} and T_{pp}^{obs}. We noticed that the parts where the reflector is closer to the free surface $\mathit{\Gamma}$, these errors are larger. One possible reason for this behaviour is that the algorithm initially converges on the shallower parts of the reflector (near the surface $\mathit{\Gamma}$), given that the curve $\phi(x, z)$ updates and moves from top to bottom. In later iterations the solution oscillates in these shallower parts, while the algorithm solves for the deeper parts of the reflector. As a final result, this test allows setting parameter $\mathit{\Psi} = 1.25$ in equation (40) so that the inverted reflector model $\phi(x, z) = 0$ converges in an optimal and stable process.

6.2. Test 2: Inversion of V_s and reflector ($\phi(x, z) = 0$) when true V_p is known

This test evaluates the performance of the presented PS tomography algorithm when true V_p is known in Ω_1: [$\boldsymbol{\phi}, \boldsymbol{V_s}$] ←**Tomo_PS-PP($\boldsymbol{\phi^{k=0}}$,$\boldsymbol{V_s^{k=0}}$,$\boldsymbol{V_p}$)**. This case is analogous to a multicomponent processing, where V_p has been determined (for instance using first arrivals tomography) and V_s is unknown.

In the first part of the experiment, the travel times T_{ps}^{obs} and T_{pp}^{obs} are determined

Figure 8

Test 1: Evolution of $\phi^k(x,z) = 0$ (reflector model) given true velocity fields V_s and V_p: $[\boldsymbol{\phi}] \leftarrow$ ***Tomo_PS-PP($\boldsymbol{\phi^{k=0}}$,$\boldsymbol{V_s}$,$\boldsymbol{V_p}$)****.*

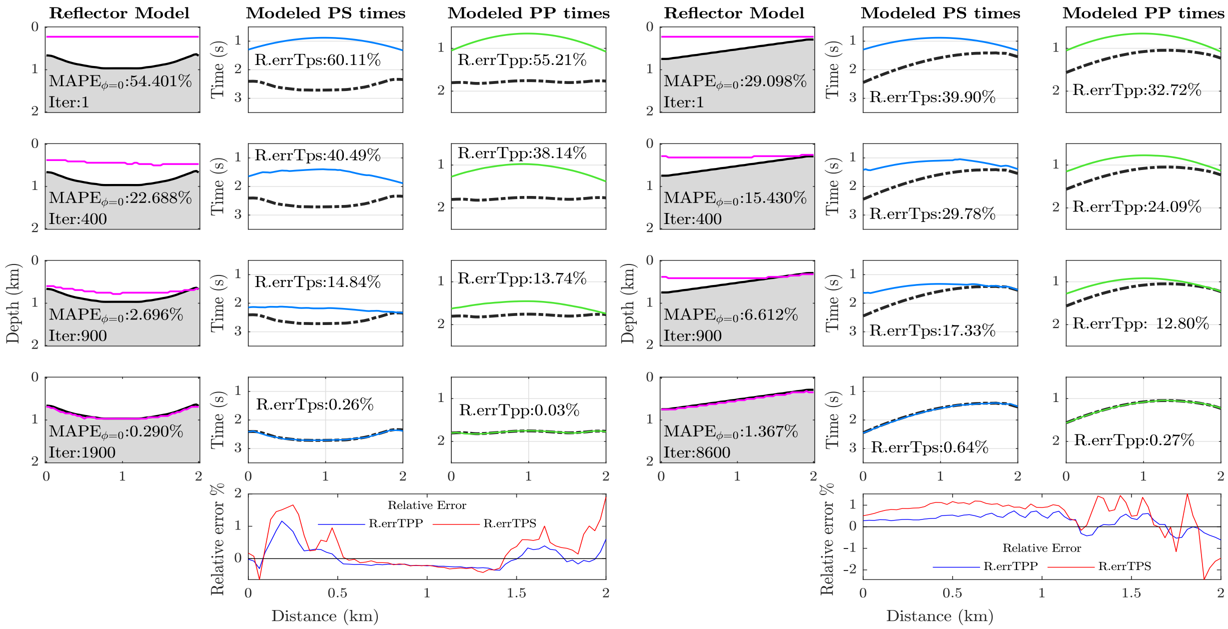

(a) Synclinal model (b) Monoclinal model

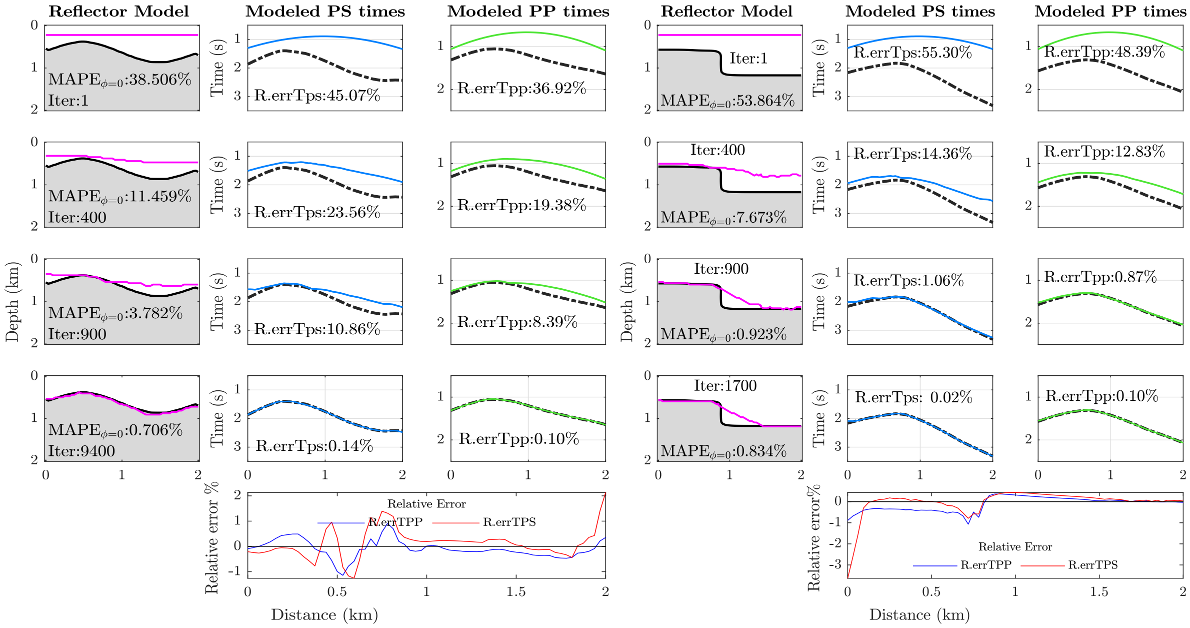

(c) Sinusoidal model (d) Step discontinuity model

Model geometry: (a) synclinal model, (b) monoclinal model, (c) sinusoidal model, (d) step discontinuity model. Each figure includes in the first column the position of $\phi^k(x,z) = 0$ in magenta for some representative iterations (k). The second column shows the average travel times of all shots for the PS wave, in dashed black line, the observed travel times and in blue the average PS modeled times. The third column shows the PP wave average observed travel times, black dotted line for travel times and in green the modeled PP travel times. In the labels inside the figures, are specified the error between the real reflector coordinates with respect to the one obtained with the inversion $\phi(x,z) = 0$ (MAPE$_{\phi=0}$: Mean absolute percent location error), the number of iterations, as well as the relative errors of the residuals of the travel times of both PS (R.errTps) and PP (R.errTpp). The bottom inset frame of the figures shows the spatial distribution of the relative errors of PS (in red) and PP (in black) travel time residuals.

Table 3
The reflector geometry with anomaly.

Model	**Velocity anomaly**
Synclinal	$\O_z = 0.4$ km, $\O_x = 1$ km, $\Delta_z = 1.5$ km, $\Delta_x = 1$ km
Monocline	$\O_z = 0.4$ km, $\O_x = 0.2$ km, $\Delta_z = 0.4$ km, $\Delta_x = 0.65$ km
Sinusoidal:	$\O_z = 0.1$ km, $\O_x = 0.2$ km, $\Delta_z = 0.4$ km, $\Delta_x = 1.5$ km

from the simulated true homogeneous models $V_s^{true} = 0.5$ km/s and $V_p^{true} = 1$ km/s in Ω_1 (defined by $\phi^{true}(x, z) = 0$), Figure 9; while in the second part they are measured on the homogeneous models with the addition of the velocity anomaly described in section 6 equation (43), Figure 10.

The set of models with velocity anomaly is defined according to the reflector geometry: for the syncline, the anomaly function is parameterized with ; for the monoclinal ; and the for sinusoidal geometry .

The algorithm for the homogeneous models is run for 50 000 iterations obtaining converging results for both $\phi(x, z) = 0$ and V_s. At each iteration the true homogeneous velocity field $V_p = 1$km/s is known for this experiment, it is not updated, it fills Ω_1, according to the evolution of $\phi^{k=0,\ldots,end}(x, z) = 0$.

The modeled reflector ($\phi^k(x, z) = 0$) converges to the different true reflectors with the syncline having the smallest error (MAPE$_{\phi=0} = 0.16$ %); while the monoclynal exhibits the largest one (MAPE$_{\phi=0} = 5.92$ %), which coincides with the shallower depth of this reflector, in a similar way to what we explained in the previous section.

The error measure for times T_{ps} and T_{pp} (R.errTps and R.errTpp) is small for all reflector geometries studied. $T_{ps}(\phi, S_{p1}, S_{s1})$ and $T_{pp}(\phi, S_{p1})$, calculated from the estimate of $V_s^{k=end}$ and the true V_p, depend on the position of the curve $\phi^k(x,z) = 0$, which compensates for errors in the shape and position of this curve with changes in velocity values within Ω_1. As a result, the inverted model of $V_s^{k=end}$ falls in the range [0.488, 0.515] km/s, around the true value of 0.5 km/s.

Figure 9-d presents the absolute percentage error (APE [5]) between the true V_s^{true} and the estimated $V_s^{k=end}$ from the proposed PS tomography. The figure indicates that the estimated $V_s^{k=end}$ model for the monocline geometry exhibits the largest $APE = 3.758\,\%$. To study the distribution of the error percentage APE, the 75 percentile (P_{75}) of the experiments is also calculated. The highest $\mathrm{P}_{75} = 3.275\,\%$ corresponding to the Monocline reflector and the lowest $0.539\,\%$ to the Sine one. The corresponding reflector position and time errors are summarized in Table 4.

A second group of experiments use true V_s models with velocity anomalies. They show how the $\phi(x,z) = 0$ reflector, try to compensate for the velocity intrusion and converge to the travel times, reaching an acceptable convergence, Figure 10. The poorest performance is for the monocline reflector, where $\mathrm{MAPE}_{\phi=0} = 10.12$ %, and the best one for the syncline geometry with $\mathrm{MAPE}_{\phi=0} = 2.19$ %.

Figure 10-d shows the spatial distribution of the APE error of the estimated velocities $V_s^{k=end}$ with respect to the V_s^{true}. The errors are maximal at the locations of the anomalies.

---

[5] $APE = |\frac{model(S_{s,p}) - true(S_{s,p})}{true(S_{s,p})}| \cdot 100$ %

Figure 9

Test 2 (homogeneous Vs): PS Tomography for homogeneous models. We simultaneously invert $\phi(x,z)$ and $V_s(x,z)$ given the true $V_p(x,z)$: $[\boldsymbol{\phi}, \boldsymbol{V_s}] \leftarrow$ ***Tomo_PS-PP***$(\boldsymbol{\phi^{k=0}}, \boldsymbol{V_s^{k=0}}, \boldsymbol{V_p})$*.*

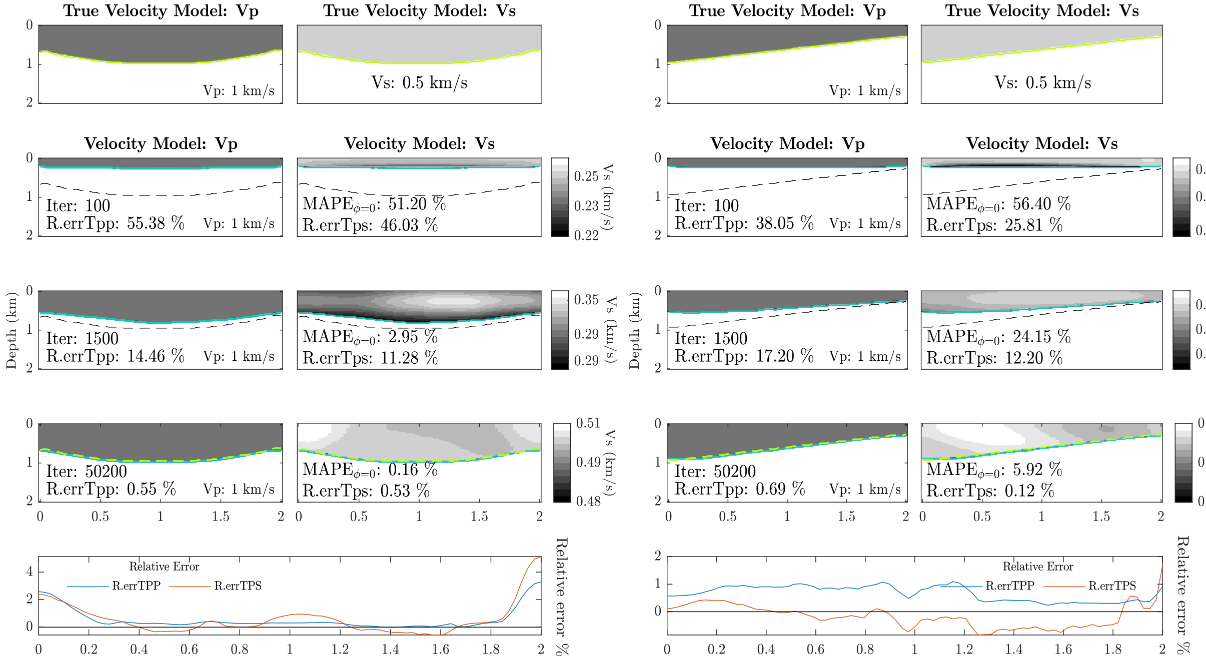

(a) Synclinal model

(b) Monoclinal model

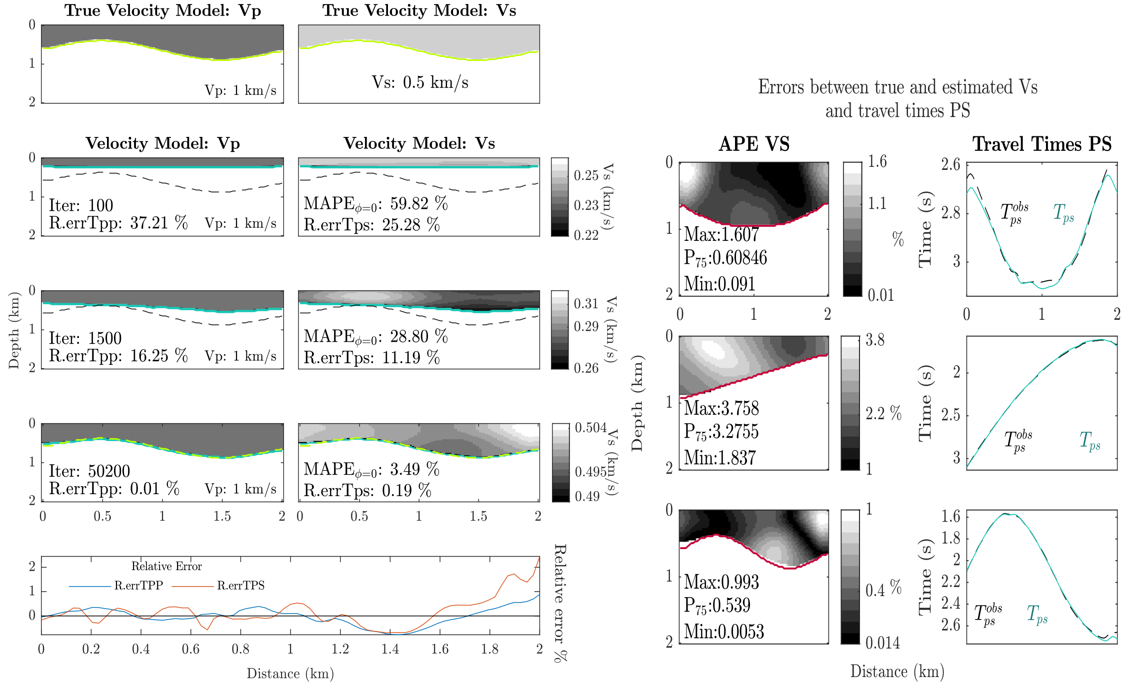

(c) Sinusoidal model

(d)

The Figures show the evolution of reflector geometry and velocities during the Tomography algorithm for different geometries: ***(a)*** *Syncline,* ***(b)*** *Monocline and* ***(c)*** *Sinusoidal. Pannel* ***(d)*** *presents the spatial distribution of the absolute percentage error (APE) between the true V_s with respect to the one produced by the tomography algorithm, within Ω_1, as well as the convergence between the observed travel times with the PS modeled ones. Notice that gray scale min and max vary to improve the visibility of results.All the other conventions follow those of Figure 8.*

Table 4

Performance figures for the inverson of ϕ and V_s in homogeneous medium with and without V_s anomaly when true V_p is known: $[\boldsymbol{\phi}, \boldsymbol{V_s}] \leftarrow$ ***Tomo_PS-PP***$(\boldsymbol{\phi^{k=0}}, \boldsymbol{V_s^{k=0}}, \boldsymbol{V_p})$.

Reflector			Homogeneous (%)		
Geometry	MAPE$_{\phi=0}$	R.errTps	R.errTpp	APE∈[min, max]	P$_{75}$
Syncline	0.16	***0.53***	0.55	[0.091, 1.607]	0.6084
Monocline	***5.92***	0.12	***0.69***	[***1.837***, ***3.758***]	***3.2755***
Sine	3.49	0.19	0.01	[0.0053, 0.993]	0.539
			Homogeneous with Anomaly (%)		
Syncline	2.19	***0.18***	***2.45***	[0.05, 9.138]	7.711
Monocline	***10.11***	0.18	3.91	[***0.8***, 22.74]	***15.149***
Sine	3.53	0.001	1.15	[0.0651, ***32.64***]	3.633

For each measured variable, the minimum (in grey) and maximum (bold) values are highlighted.

The sine reflector model has the largest error 32.64 %, while the highest P$_{75}$ is 15.149 % corresponding to the Monocline reflector. Similarly, traveltimes $T_{ps}(\phi, S_{p1}, S_{s1})$ and $T_{pp}(\phi, S_{p1})$ converge but, as expected, with larger errors than for the homogeneous models. Table 4 compares the errors between homogeneous and anomaly case.

As an additional result, during test 2, it was determined that the update of S_s in equation (42) stably converges with $\zeta = 0.125$.

6.3. Test 3: Inversion of V_p and reflector $(\phi(x, z) = 0)$ when V_s is known

In this case, the velocity field V_s^{true} is fixed and the tomography algorithm estimates V_p^k and the position and shape of the reflector, $\phi(x, z) = 0$: $[\boldsymbol{\phi}, \boldsymbol{V_p}] \leftarrow$**Tomo_PS-PP**$(\boldsymbol{\phi^{k=0}}, \boldsymbol{V_s}, \boldsymbol{V_p^{k=0}})$. For the experiments with homogeneous models and those with the anomaly, the initial model is defined as: $V_p^{k=0} = 0.5$ km/s and $V_s^{true} = 0.5$ km/s and the

Figure 10

Test 2 (heterogenous Vs): PS Tomography for models with overlapping velocity anomaly. We simultaneously invert $\phi(x,z)$ and $V_s(x,z)$ given the true $V_p(x,z)$ models:$[\boldsymbol{\phi}, \boldsymbol{V_s}] \leftarrow$ ***Tomo_PS-PP****$(\boldsymbol{\phi^{k=0}}, \boldsymbol{V_s^{k=0}}, \boldsymbol{V_p})$.*

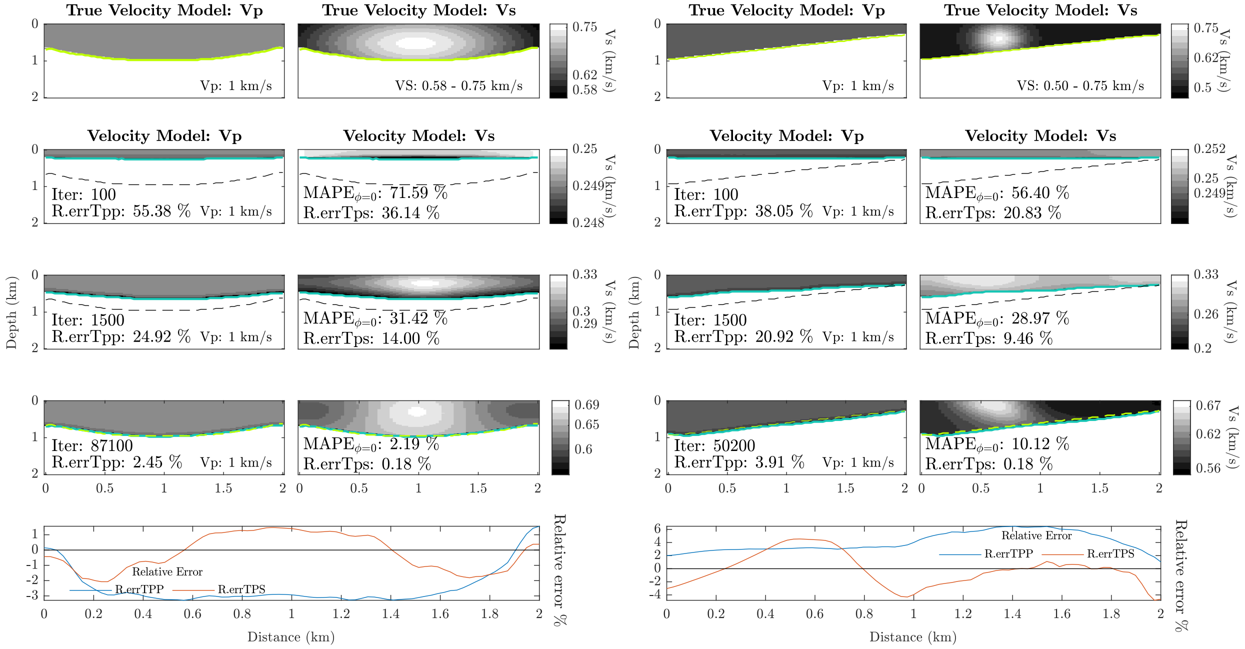

(a) Synclinal model (b) Monoclinal model

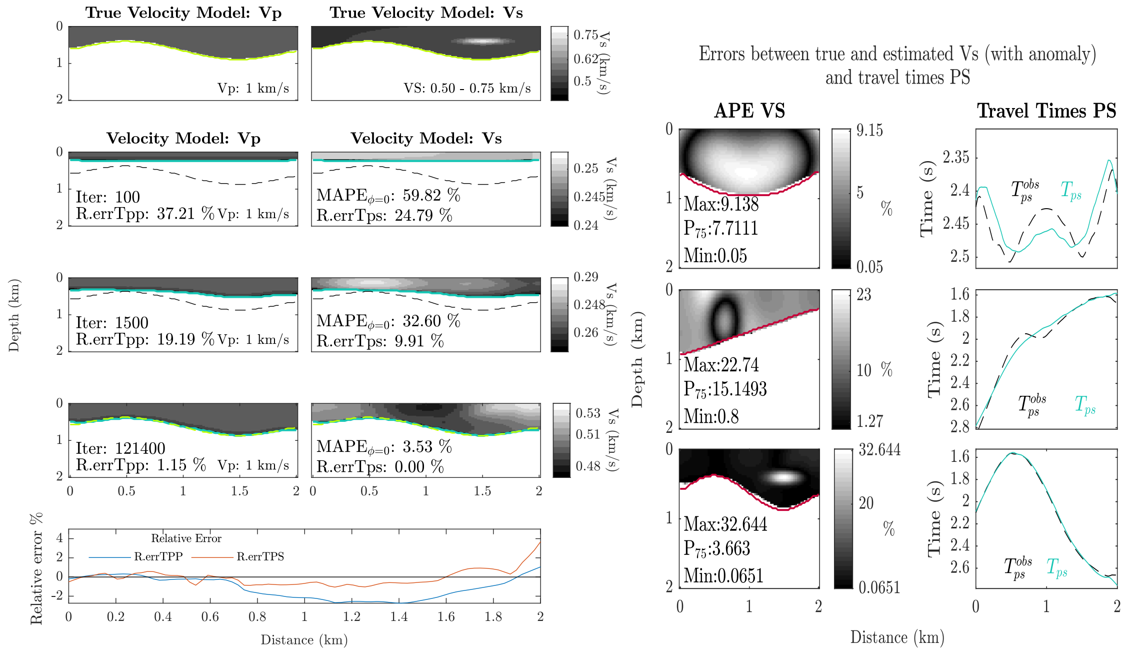

(c) Sinusoidal model (d)

All the other conventions follow those of Figure 8. The Figures show the evolution of the Tomography algorithm for different geometries: ***(a)*** *Syncline,* ***(b)*** *Monocline,* ***(c)*** *Sinusoidal, while* ***(d)*** *presents the spatial distribution of the absolute percentage error (APE) between the true V_s with respect to the one produced by the tomography algorithm, within Ω_1, is shown, as well as the convergence between the observed travel times with the PS modeled ones. Notice that gray scale min and max vary to improve the visibility of results..*

initial model of the reflector is set as in the previous experiments. This case is analogous with a complement to multichannel analysis of surface waves (MASW) type processing, where the V_s has been determined and V_p is to be estimated or calibrated.

The inverted $\phi^k(x,z) = 0$ model converges to the $\phi^{true}(x,z) = 0$ reflector less accurately than in the previous experiments, see Figure 11. In this case, the errors for each geometry are: sine reflector $\text{MAPE}_{\phi=0} = 3.37$ %, monocline $\text{MAPE}_{\phi=0} = 3.59$ % and the syncline $\text{MAPE}_{\phi=0} = 1.9$ %.

There is a good convergence of travel times, especially good for the syncline reflector. The relative error $R.errTPP = 2.51\%$ is the largest for the sine reflector, for which the velocities within Ω_1 are in the range $[0.93, 0.96]$ km/s thus underestimating the 1km/s true velocity.

For this experiment 150 000 iterations are are completed, ≈3 times more than for the previous tests. Figure 11-d presents the APE absolute percentage error between the true V_p and those estimated by the algorithm. The monocline geometry exhibits the largest errors [0.076, 9.3] %, while the highest P_{75} is 5.5271 % corresponding to the sine reflector. Whereas the one with the smallest errors is the syncline one [1.62, 2.94] %, with a P_{75} of 2.5751 %.

In this test, the velocity anomaly for the Syncline model was modified from the previous ones, so that the anomaly is more compact by setting $\O_x = 0.4$ km.

The results for the velocity anomaly models show that the anomaly has a compensating effect on the shape and position of the reflector, to minimise the energy function based on the PS-PP traveltime residuals, see Figure 12. In these results, the largest shape error

Figure 11

Test 3 (Homogeneous Vp): PS Tomography for Homogeneous models. We simultaneously Invert both $\phi(x,z)$ *and* $V_p(x,z)$ *given the true* $V_s(x,z)$*:* $[\boldsymbol{\phi}, \mathbf{V_p}] \leftarrow$ ***Tomo_PS-PP***$(\boldsymbol{\phi^{k=0}}, \mathbf{V_s}, \mathbf{V_p^{k=0}})$

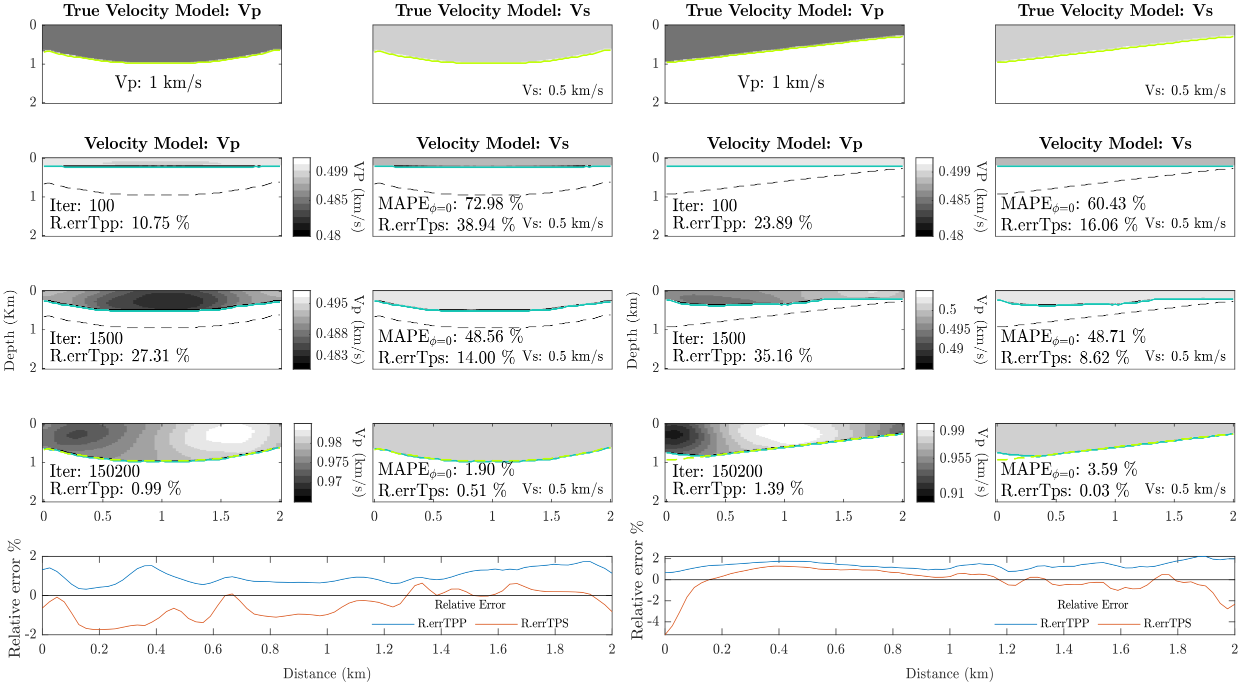

(a) Synclinal model (b) Monoclinal model

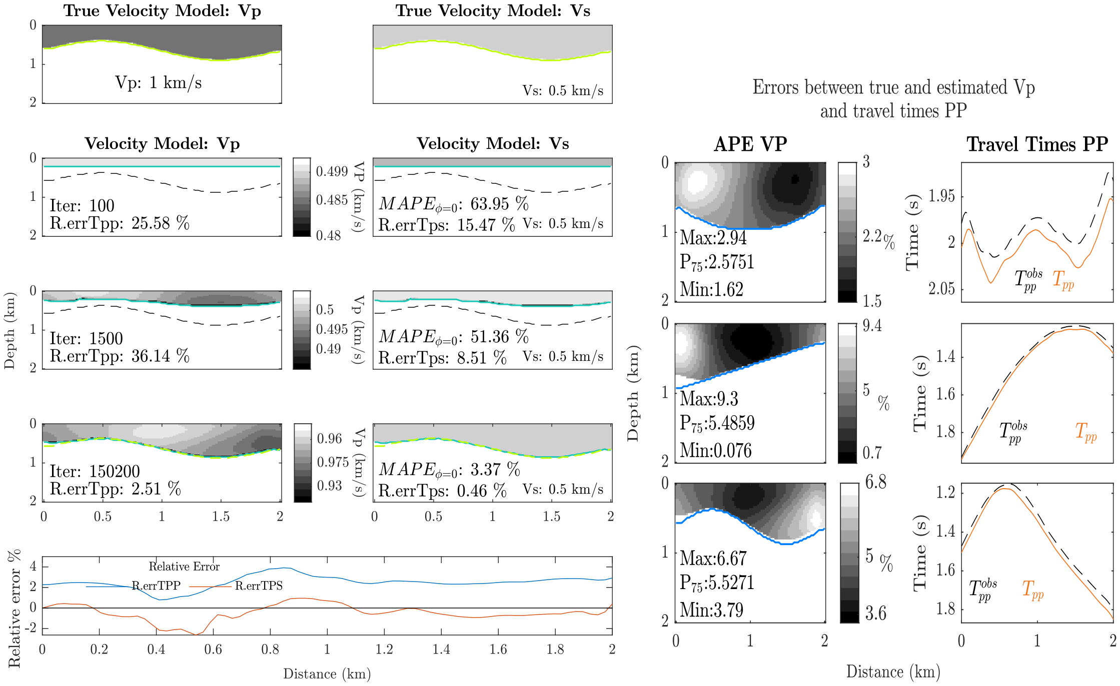

(c) Sinusoidal model (d)

The Figures show the evolution of the Tomography algorithm for different geometries: ***(a)*** *Syncline,* ***(b)*** *Monocline,* ***(c)*** *Sinusoidal.* ***(d)*** *presents the spatial distribution of the absolute percentage error (APE) between the true* V_s *with respect to the one produced by the tomography algorithm, within* Ω_1*, is shown, as well as the convergence between the observed travel times with the PS modeled ones. Notice that gray scale min and max vary to improve the visibility of results. All the other conventions follow those of Figure 8.*

Table 5

Performance figures for the inverson of ϕ and V_p in homogeneous medium with and without V_p anomaly when true V_s is known: [$\boldsymbol{\phi}, \boldsymbol{V_p}$] $\leftarrow$ ***Tomo_PS-PP(***$\boldsymbol{\phi^{k=0}}$***,***$\boldsymbol{V_s}$***,***$\boldsymbol{V_p^{k=0}}$***)***.

Reflector			Homogeneous (%)		
Geometry	MAPE$_{\phi=0}$	R.errTps	R.errTpp	APE$\in$[min, max]	P$_{75}$
Syncline	1.9	***0.51***	0.99	[1.62, 2.94]	2.5751
Monocline	***3.59***	0.03	1.39	[0.076, ***9.3***]	5.4859
Sine	3.37	0.45	***2.51***	[***3.79***, 6.67]	***5.5271***
			Homogeneous with Anomaly (%)		
Syncline	3.14	***1.8***	***3.05***	[***1.87***, ***30.92***]	***9.9056***
Monocline	3.1	1.29	2.36	[0.001, 19.96]	5.4689
Sine	***5.08***	1.58	2.01	[0.069, 18.3]	7.2676

For each measured variable, the minimum (in grey) and maximum (bold) values are highlighted.

occurs in the sinusoidal reflector geometry with a MAPE$_{\phi=0}$ of 5.09

As the shape of the reflector is distorted, the velocity compensation makes the original anomaly indistinguishable, so the errors in $T_{ps}(\phi, S_{p1}, S_{s1})$ and $T_{pp}(\phi, S_{p1})$ are larger than for the previous tests, with the largest error being $R.errTpp = 3.05\%$ and $R.errTps = 1.8\ \%$ in the Syncline model.

Figure 12-d presents the spatial behavior of the absolute percentage error APE of the P velocities over Ω_1, where the maximum error for all three geometries is around 30.9 % with a P$_{75}$ of 9.9056 % for the syncline reflector, which takes place in the area where the V_p anomaly is located. Table 5 compares the inversion results for the different geometries. As an additional result, this test allow to estimate the update factor for Sp, $\boldsymbol{\eta}$ in equation (41), is heuristically found to be $\eta = 0.025$.

Figure 12

Test 3 (heterogenous Vp): PS Tomography for Homogeneous models with overlapping velocity anomaly. We simultaneously Invert both $\phi(x,z)$ and $V_p(x,z)$ given the true $V_s(x,z)$ models with anomaly: $[\boldsymbol{\phi}, \boldsymbol{V_p}] \leftarrow$ ***Tomo_PS-PP***$(\boldsymbol{\phi^{k=0}}, \boldsymbol{V_s}, \boldsymbol{V_p^{k=0}})$. *The convergence iteration number (Iter), the relative error between observed and modeled travel times for both PP (R.errTpp) and PS (R.errTps) are displayed.*

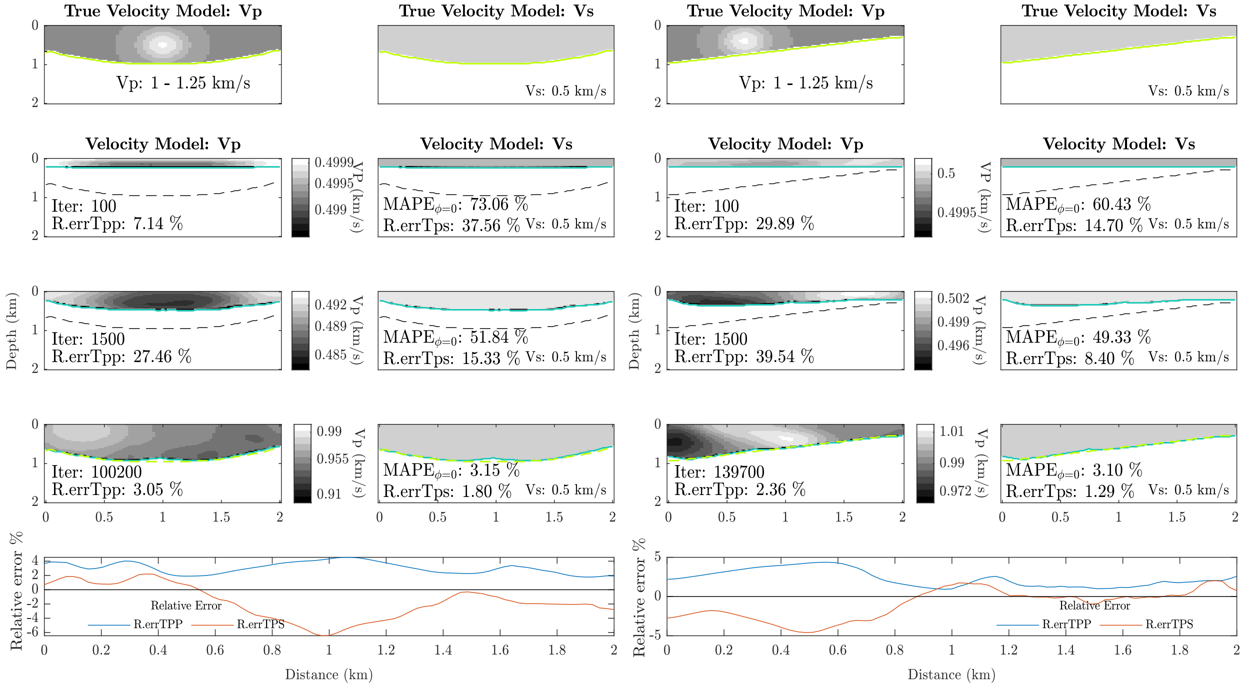

(a) Synclinal model

(b) Monoclinal model

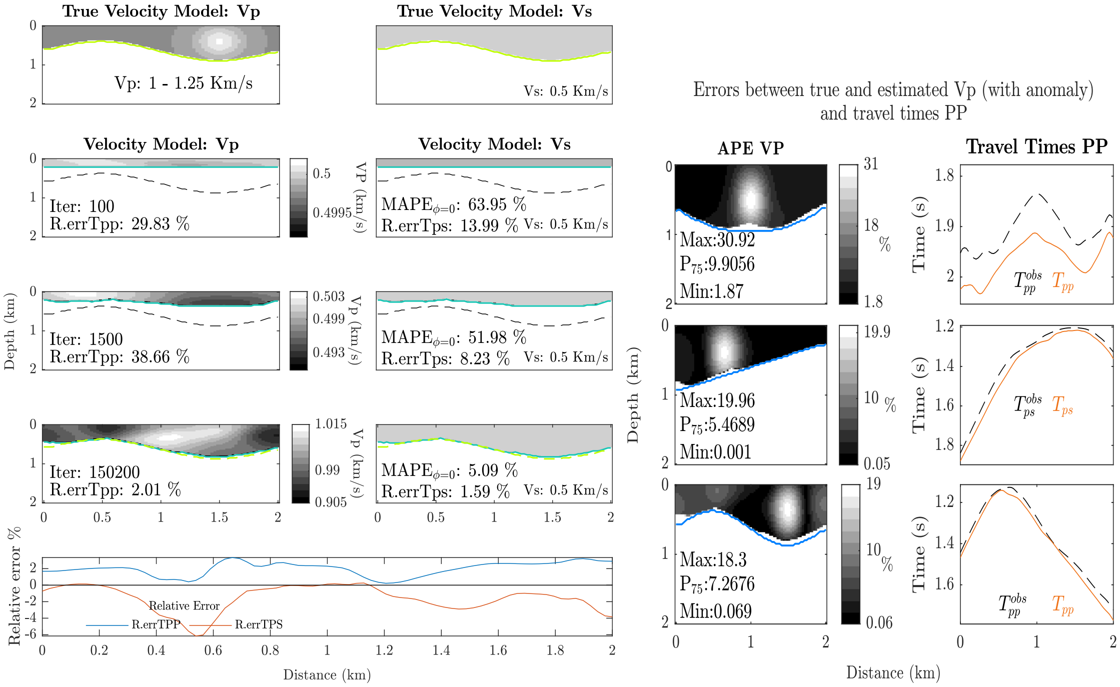

(c) Sinusoidal model

(d)

The Figures show the evolution of the Tomography algorithm for different geometries: ***(a)*** *Syncline,* ***(b)*** *Monocline, and* ***(c)*** *Sinusoidal.* ***(d)*** *presents the spatial distribution of the absolute percentage error (APE) between the true V_p with respect to the one produced by the tomography algorithm, within Ω_1, is shown, as well as the convergence between the observed travel times with the PS modeled ones.*

6.4. Test 4: Inversion tomography of V_s, V_p, and reflector $\phi(x, z) = 0$

Finally, the PS converted wave tomography process is performed simultaneously on the three fields: location and shape of the reflector $\phi^{k=0}(x, z)$, V_s^k and, V_p^k, for homogeneous models and with velocity anomaly. This test is more affected by illumination effects than the previous ones. Within the illuminated area, the reflector and inverted velocities converge well; the values of homogeneous model inversions, for the three reflector geometries, fluctuate in the range $[0.65, 1.1]$ km/s for V_p^{true} (1 km/s), and $[0.4, 0.52]$ km/s (being 0.5 km/s) for V_s^{true}. The measured difference between the true reflector and the estimated one $\phi^k(x, z) = 0$ ($\text{MAPE}_{\phi=0}$) is on average about 13%, values that are largely controlled by the spatial distribution of the illumination (Please see the Discusion section) which prevents an accurate recovery of the true reflector, see Figure 13.

Figure 13-d presents the spatial distribution of the APE absolute percentage error for $V_s^{k=end} - V_s^{true}$ as well as for $V_p^{k=end} - V_p^{true}$. It can be seen that the maximum error for field S is exhibited by the sine reflector, with a value of 44.02 % and a P_{75} of 15.27 %, while for the P velocity field the maximum error is 45.50 % corresponding to the sine reflector, with a P_{75} of 26.98 %. It can also be noted how $T_{ps}(\phi, S_{p1}, S_{s1})$ and $T_{pp}(\phi, S_{p1})$ times converge very close to the observed ones.

For the simulations with velocity anomalies, three reflector geometries are defined as in the previous experiments. The velocity anomaly defined in Section 6 is added to the true homogeneous model $V_p^{true} = 1$ km/s. Given the V_p we define $V_s = \frac{V_p}{3}$, following an average

Figure 13

*Test 4 (homogeneous Vp and Vs): PS tomography for Homogeneous models. Simultaneous inversion of $\phi(x,z)$, $V_s(x,z)$ and $V_p(x,z)$: $[\boldsymbol{\phi}, \boldsymbol{V_s}, \boldsymbol{V_p}] \leftarrow$ **Tomo_PS-PP**$(\boldsymbol{\phi^{k=0}}, \boldsymbol{V_s^{k=0}}, \boldsymbol{V_p^{k=0}})$. The convergence iteration number (Iter), the relative error between observed and modeled times, is presented for both PP (R.errTpp) and PS (R.errTps).*

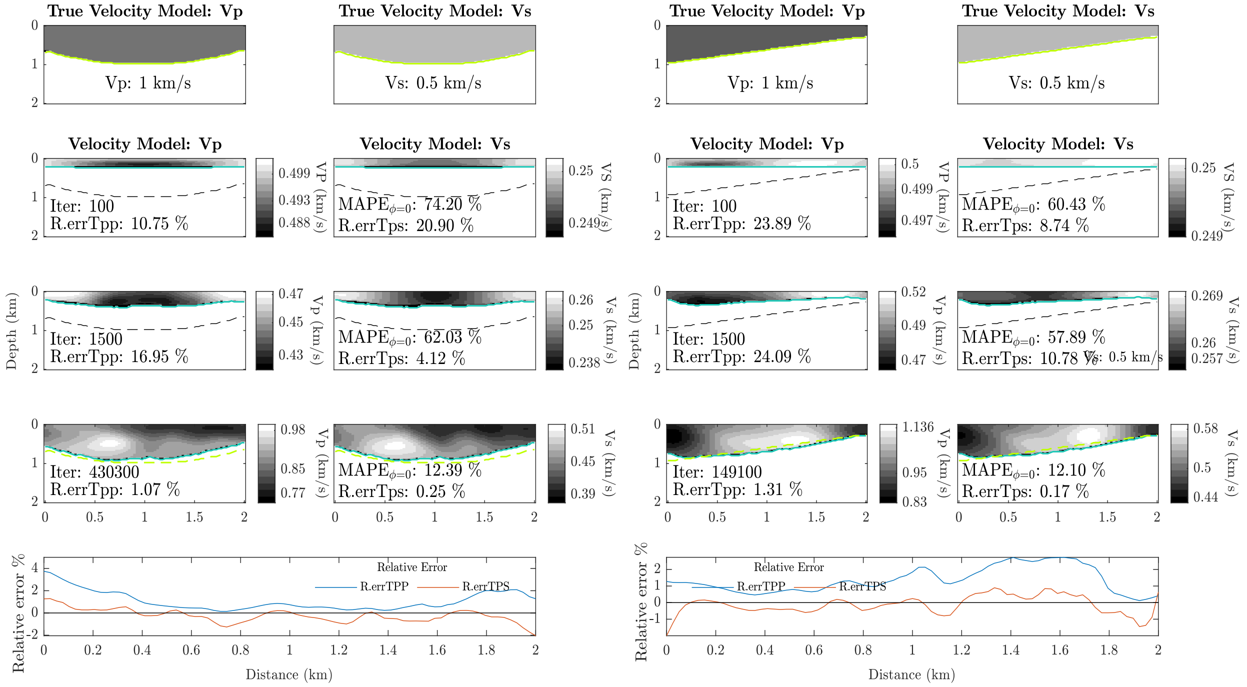

(a) Synclinal model (b) Monoclinal model

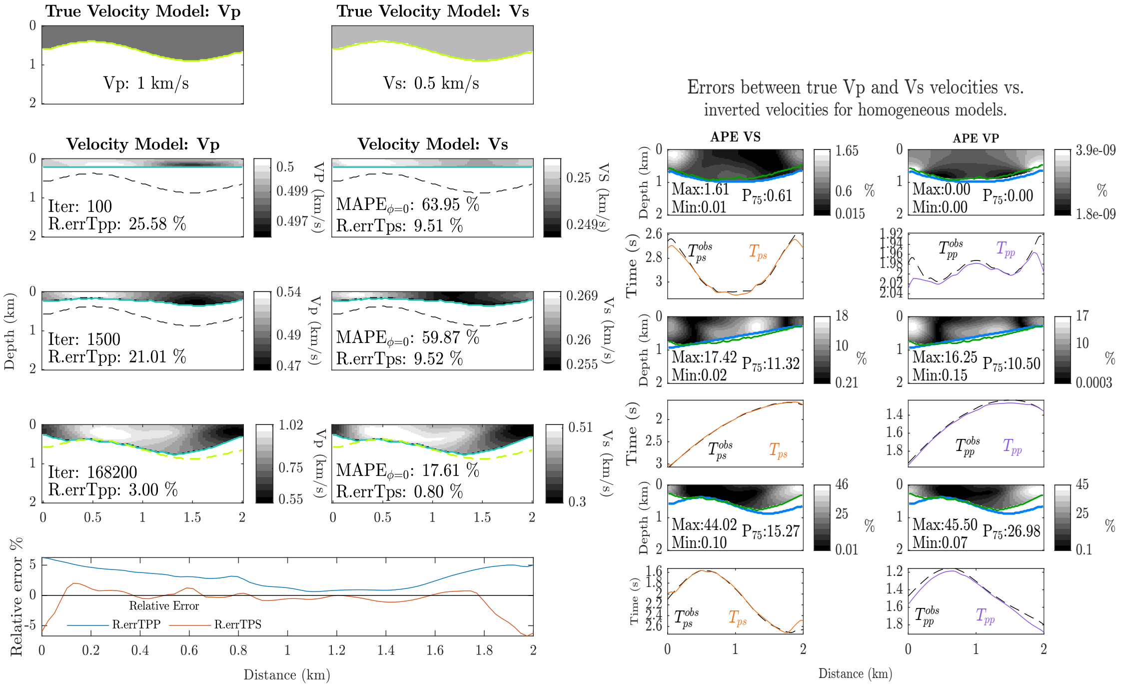

(c) Sinusoidal model (d)

*The Figures show the evolution of the Tomography algorithm for different geometries: **(a)** Syncline, **(b)** Monocline, and **(c)** Sinusoidal. **(d)** presents the Absolute Percentage Error (APE) between the true velocities V_s-V_p with respect to the inversion performed by the proposed tomography algorithm of V_s and V_p within Ω_1 are shown, also the convergence between the observed travel times with both PP and PS modeling is shown. Note the effects of border illumination in the error in the estimated position of the reflector.*

V_p/V_s ratio generally found in near surface. Please observe the first rows of all images in Figure 14.

The initial models of the reflector and velocities are defined as in the previous tests: $V_s^{k=0} = 0.25$ km/s, $V_p^{k=0} = 0.5$ km/s, and a flat initial reflector $\phi^{k=0}(x, z) = 0$ located at 20 m from the $\mathit{\Gamma}$ surface, see second row in each part of Figures 13 and 14.

In contrast to the previous tests, the intrusion in the inversion causes the reflectors ($\phi(x, z) = 0$) to converge trying to compensate the velocity anomaly by modifying the shape of the reflector as is evidenced in Figure 14. Again, the illumination causes the reflector to be mapped only in one region. In this test, the algorithm requires a large number of iterations, between 200 000 and 750 000.

The shape distortion of $\phi(x, z) = 0$ (compensating for the velocity anomaly) is most evident when the reflector geometry is monocline, see Figure 14-b. The V_s^{true} and V_p^{true} models with immersed anomaly in the syncline geometry estimated by the developed tomography resemble the true ones, even where the anomaly is located, see Figure 14-a. For the other reflector geometries, the velocity models do not recover the velocity anomaly.

For the illuminated areas, the velocities (both V_p and V_s) converge to some extent to the true ones, for the syncline model $V_p \in [0.85, 1.007]$ km/s and $V_s \in [0.27, 0.33]$ km/s , for the sine reflector $V_p \in [0.8, 1.02]$ km/s and $V_p \in [0.25, 0.32]$ km/s, and finally for the monocline $V_p \in [1.01, 1.23]$ km/s and $V_s \in [0.33 - 0.45]$ km/s; measurements that should converge to the true $V_p \in [1, 1.25]$ km/s and $V_s \in [0.33, -0.42]$ km/s for the syncline and sinusoid, while for the monocline $V_p \in [1, 1.5]$ km/s and $V_s \in [0.33, 0.5]$ km/s, see Figure 14.

T_{ps} and T_{pp} converge to the observed times, Figure 14-d presents these trends. While the APE errors for the models with an anomaly for the S field present their maximum for the sine reflector 45.07 % with a P_{75} of 24.789 %, being for the P field the maximum 73.45 %, with a P_{75} of 23.32 % for the sine reflector. The update parameters described in the equation (41) were previously determined in the previous test as: $\Psi = 1.25$, $\zeta = 0.125$ and $\eta = 0.025$. Table 6 shows a comparison of the error measures for this test.

Figure 14

Test 4 (heterogeneous): PS tomography for Homogeneous models with overlapping velocity anomaly. Simultaneous inversion of $\phi(x,z)$, $V_s(x,z)$ *and* $V_p(x,z)$*:* $[\boldsymbol{\phi}, \boldsymbol{V_s}, \boldsymbol{V_p}] \leftarrow \textbf{\textit{Tomo\_PS-PP}}(\boldsymbol{\phi^{k=0}}, \boldsymbol{V_s^{k=0}}, \boldsymbol{V_p^{k=0}})$*. The convergence iteration number (Iter), the relative error between observed and modeled times, is given for both PP (R.errTpp) and PS (R.errTps).*

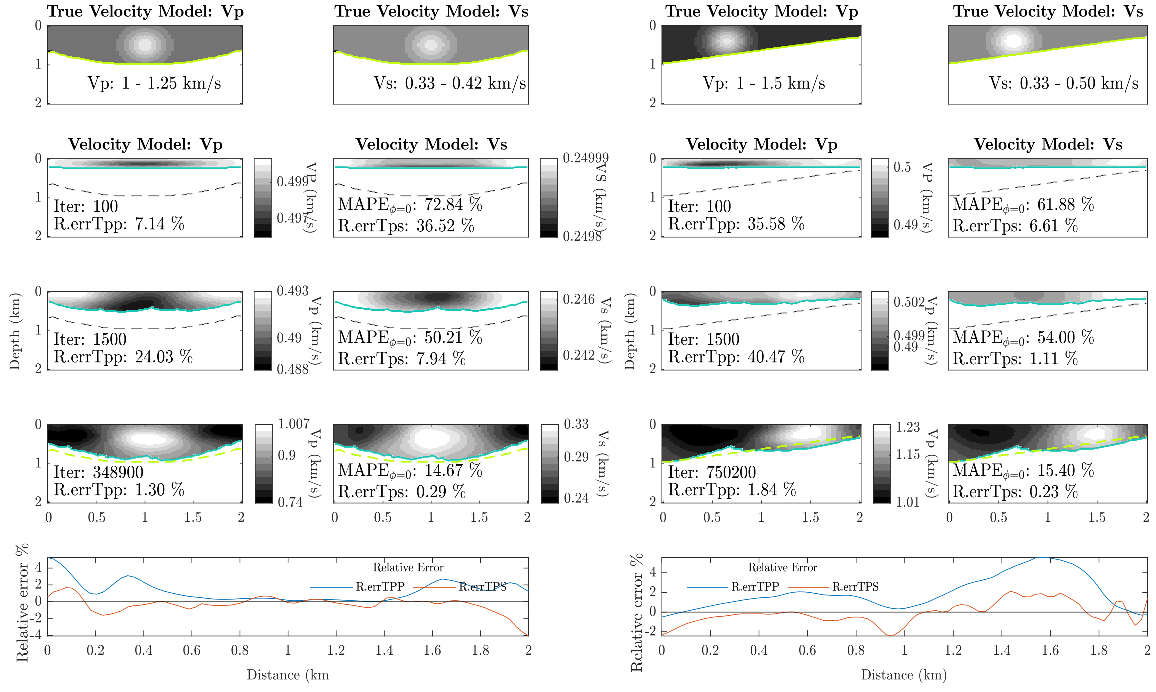

(a) Synclinal model

(b) Monoclinal model

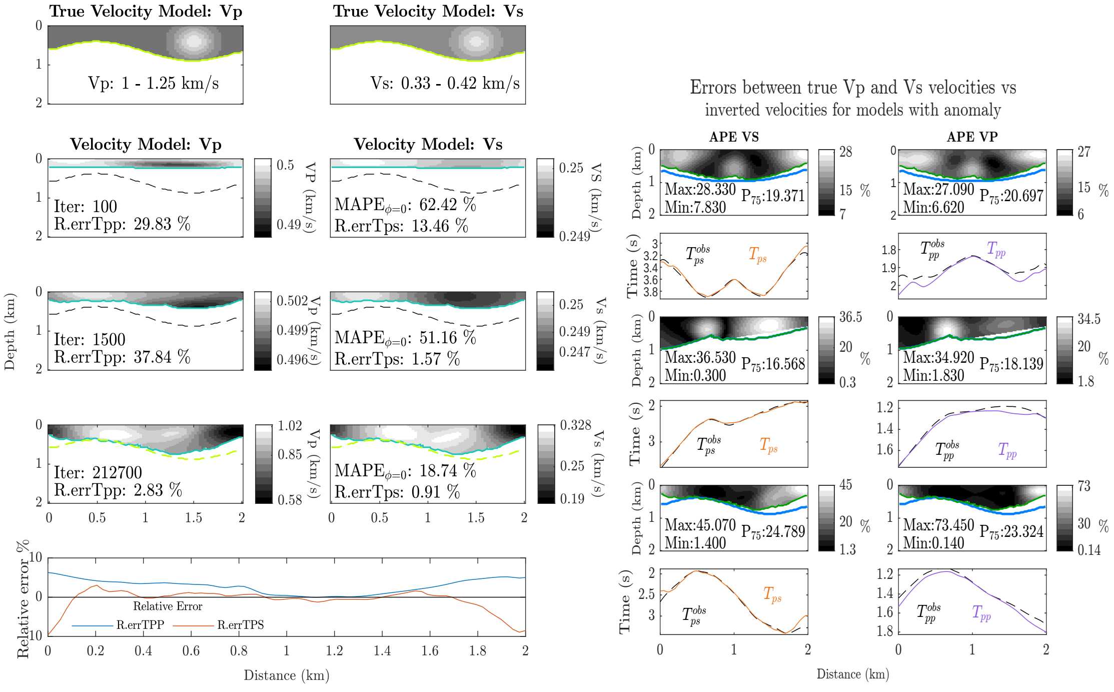

(c) Sinusoidal model

(d)

Figures show the evolution of the Tomography algorithm for different geometries: ***(a)*** *Syncline,* ***(b)*** *Monocline, and* ***(c)*** *Sinusoidal.* ***(d)*** *presents the Absolute percentage error (APE) between the true velocities* V_s*-*V_p *with respect to the inversion performed by the proposed tomography algorithm of* V_s *and* V_p *within* Ω_1 *are shown, also the convergence between the observed travel times with both PP and PS modeling is shown. Here there is a combined effect of border illumination and velocity anomaly compensation for the error in the estimated position of the reflector.*

Table 6

*Performance percentage errors for the inversion of ϕ, V_p, and V_s in homogeneous medium with and without anomaly on V_P and V_s: $[\boldsymbol{\phi}, \boldsymbol{V_s}, \boldsymbol{V_p}] \leftarrow$ **Tomo_PS-PP**$(\boldsymbol{\phi^{k=0}}, \boldsymbol{V_s^{k=0}}, \boldsymbol{V_p^{k=0}})$.*

	Homogeneous V_s and V_p (%)			
Reflector Geometry	$\text{MAPE}_{\phi=0}$	R.errTps	R.errTpp	
Syncline	12.39	0.25	1.07	
Monocline	12.10	0.17	1.31	
Sine	**17.61**	**0.8**	**3**	
	V_s		V_p	
	APE∈[min, max]	P_{75}	APE∈[min, max]	P_{75}
Syncline	[0.01, 1.610]	0.61	[0.00, 0.000]	0
Monocline	[0.02, 17.42]	11.32	[**0.15**, 16.25]	10.5
Sine	[**0.10**, **44.02**]	**15.27**	[0.070, **45.50**]	**26.98**
	Homogeneous with Intrusive V_s and V_p (%)			
	$\text{MAPE}_{\phi=0}$	R.errTps	R.errTpp	
Syncline	14.67	0.29	1.30	
Monocline	15.40	0.23	1.84	
Sine	**18.74**	**0.91**	**2.83**	
	V_s		V_p	
	APE∈[min, max]	P_{75}	APE∈[min, max]	P_{75}
Syncline	[**7.83**,28.33]	19.371	[**6.62**, 27.09]	**29.697**
Monocline	[0.30, 36.53]	16.568	[1.83, 34.92]	18.139
Sine	[1.40, **45.07**]	**24.789**	[0.14, **73.45**]	23.324

For each measured variable, the minimum (in grey) and maximum (bold) values are highlighted.

7. Discussion

In contrast to other related works, such as Zheglova and Farquharson (2012) and Li et al. (2014), where the data come from a crosswell acquisition geometry, the algorithm we propose is intended for multicomponent surface seismic acquisition geometries, so that the designed PS-PP tomography faces amore difficult ill-posed problem. Since the multicomponent acquisition provides both S-shear and P-compressional waves information hopefully, models of P-field and S-field velocities can be reconstructed. The Tomography presented as **Tomo_PP-PS($\boldsymbol{\phi^{k=0}}$,$\boldsymbol{V_s^{k=0}}$,$\boldsymbol{V_p^{k=0}}$)**, can use previously estimated variables, either $\boldsymbol{V_s^{k=0}}$,$\boldsymbol{V_p^{k=0}}$ or $\boldsymbol{\phi^{k=0}}$ as solution, which reduce the solution of space dimensionality the problem. For example, conventional first arrival time tomography can give an approximate solution for V_p, which can be considered known for a V_s and ϕ inversion. Another idea is to follow a multistage procedure, where each parameter is solved in alternate steps. Different experiments are proposed (see Section 6), thinking also on tuning the convergence of the tomography by updating the adjustment parameters Ψ, ζ and η.

At the same time as the inversion progresses, it is necessary to use a filter to smooth the velocity models directly, as described in Wang et al. (2022). This process is necessary to prevent that the shape of the reflector in each iteration $\phi^{k=0,\ldots,end}(x,z)$ slighly drive and generate artifacts on the spatial distribution of the estimated models $V_p^{k=0,\ldots,end}$ and $V_s^{k=0,\ldots,end}$.

The new tomography method allows stable modeling of the location and shape of the reflector, using as a model $\phi(x,z) = 0$. To test the stability of the reflector inversion, we perform a test where V_s and V_p are fixed with the true values. These results are presented in the numerical test section 6.1. The travel time residuals converge almost perfectly to zero, see Figure 8. Despite having the true V_s and V_p, the effects of illumination coming from the limited the acquisition geometry, can be seen at the deepest and shallowest points in each reflector geometry, see relative error in Figure 8 Section 6.1.

The numerical test in the Section 6 demonstrates that, when a velocity anomaly is superimposed to the homogeneous models, the $\phi(x,z) = 0$ reflector fails to fully represent the true one, the velocity anomaly causes the modeled times to converge to the observed times before the reflector model ($\phi(x,z) = 0$) converges to the true one. This suggest that the updating parameters, $\mathit{\Psi}$, ζ and η, should be approached in a different way, see Sections 6.2 and 6.3, Figures 10 and 12. In the case of heterogeneous velocities, clearly those three parameters are not independent and have crossover effects (i.e. the reflector geometry update must have into account the velocity field update). Please keep in mind that we estimate those parameters in succesive tests with homogeneous models, introducing one additional parameter independently at a time in each test, and keeping the previous updating parameters fixed.

The spatial distribution of the illumination over Ω_1 is presented in Figure 15 for the PS and PP fields, given the acquisition geometry: surface receivers and sources used common for all the different tests described. It can be seen how the PS field has a larger aperture than the PP illumination, for the studied reflector geometries. It is shown that, as depth increases, the illumination on the reflector decreases. In reflector geometries with concavities (sinusoidal and syncline), PP reflections intersect with PS conversions within Ω_1 and the illumination is non-uniform (spurious stripes appear), possibly associated with the curve discretization, while in straight reflecting surfaces, such as the monocline, the illumination is smooth.

However, the result obtained in Section 6 by using the proposed tomography suggests that the inversion procedure, using the adjoint state (Lagrange multipliers) dual to the Eikonal equation, gives rise to an illumination factor, as described in Hu et al. (2021); These authors introduce an illumination compensation, by modifying the boundary condition of the adjoint state equation, obtain normalized gradient directions of the misfit functional, and use regularizer with spatially varying factors. Therefore, a possible improvement to our proposed PS-PP tomography methodology is to implement these findings.

On the other hand, for the studied reflector geometries, a distinctive feature are the reflector depths, being for the sinusoidal and moncline in the range [0.5, 1] km, while for the syncline they are in the range [0.64, 1] km. This feature leads to convergence in fewer iterations at the shallower points, so that in subsequent iterations the convergence of the velocity models may move away trying to compensate for the shape of the reflector ($\phi = 0$), especially when all three model variables are inverted at the same time. If a velocity (V_s or V_p) is known that mitigates the impact of this effect.

The convergence rate of the inversion performed by the proposed PS-PP tomography is low, since the illumination is irregular (Figure 15) for both PP and PS fields (the illumination for transmitted P field is more uniform): the adjoints (gradients) that update the velocity models (V_s, V_p) present singularities and a higher number of iterations is required to achieve convergence. Thus, reducing the non-uniformity of the illuminations produces smooth adjoints, making the velocities V_s and V_p evolve to smooth models without singularities. In this sense, a new methodology that preconditions the gradient determined by the tomography to eliminate the uneven illumination in the gradient is proposed in Zhang et al. (2023), results indicate that it can be useful in proposed tomography methodology.

Since the objective function is based on the measurement of PP and PS travel time residuals, another important aspect is the trade-off between Ω_1 shape, defined with the $\phi(x, z) = 0$, and the V_s and V_p fields of the medium. This is analogous to the velocity-depth ambiguity in seismic imaging. Thus, looking for a suitable spatial distribution of the velocities over Ω_1, we prioritize the fastest evolution of the parameter Ψ (that controls the interface $\phi(x, z)$) in the inversion process (update equations (40) , (42), and (41)). Once $\mathit{\Psi}$ is estimated, the η and ζ updating parameters of the velocity models are tuned so that the objective function converges.

It can be highlighted how the averages of the travel times, for the 49 shots, of the PS waves converge to the observed ones with small errors, while the PP ones converges with higher errors, see Figures 13 and 14. A possible improvement to the developed methodology is to redefine the initial reflector, flat in the present study, with a shape described by the averages of the travel times of the PS-wave first arrivals. This could contribute to an earlier and better quality convergence.

Another possible improvement to the proposed method is to adjust the updating parameters $\varPsi$, η, and ζ, using techniques such as L-BFGS (quasi-Newton) in a multiparametric way, seeking to decrease the number of convergence iterations, as well as to improve the spatial distribution of the error between the estimated and true models V_s and V_p. It is important to take special care of the noise in the data, since the L-BFGS method needs high quality gradients to ensure that a convex quadratic model performs searches on reliable lines Liu and Nocedal (1989). Since the proposed inversion is based on the measurement of conversion and reflection times, which in turn construct pairs of adjoint operators (cross errors), the search for minima may not be over a line, as suggested by the work of Bollapragada et al. (2018), where the use of stochastic line searches is proposed. The use of these techniques is suggested to improve the estimation of $\varPsi$, η, and ζ.

While the simultaneous inversion of ϕ, V_p, and V_s achieves acceptable results, its performance can be improved by implementing novel techniques to both handle regularization and include an illumination parameter within the adjoint computation process, so that the solution does not contain discontinuities that are not part of the physical reality; as in Bollapragada et al. (2018).

As a final remark, the designed PS-PP tomography methodology can be extended for more than one reflector. The arrival times identified on the shot gather corresponding to the PP and PS reflections produced in the second or other reflectors can be pecked to obtain new T_{ps}^{obs} and T_{pp}^{obs}, while the transmission traveltimes of the PS-PP waves calculated from the velocity models V_s and V_p over the Ω_1 region arriving on the reflector ($\phi = 0$) are considered as new sources illuminating the next Ω_2 area. Thus, the calculation of adjoint

Figure 15

Illumination distribution over Ω_1, achieved using an acquisition geometry with 49 sources at a depth of 50 meters distributed over a distance of 2 km and 79 surface receivers. The methodology followed to obtain follows the methodology is described in Li et al. (2014).

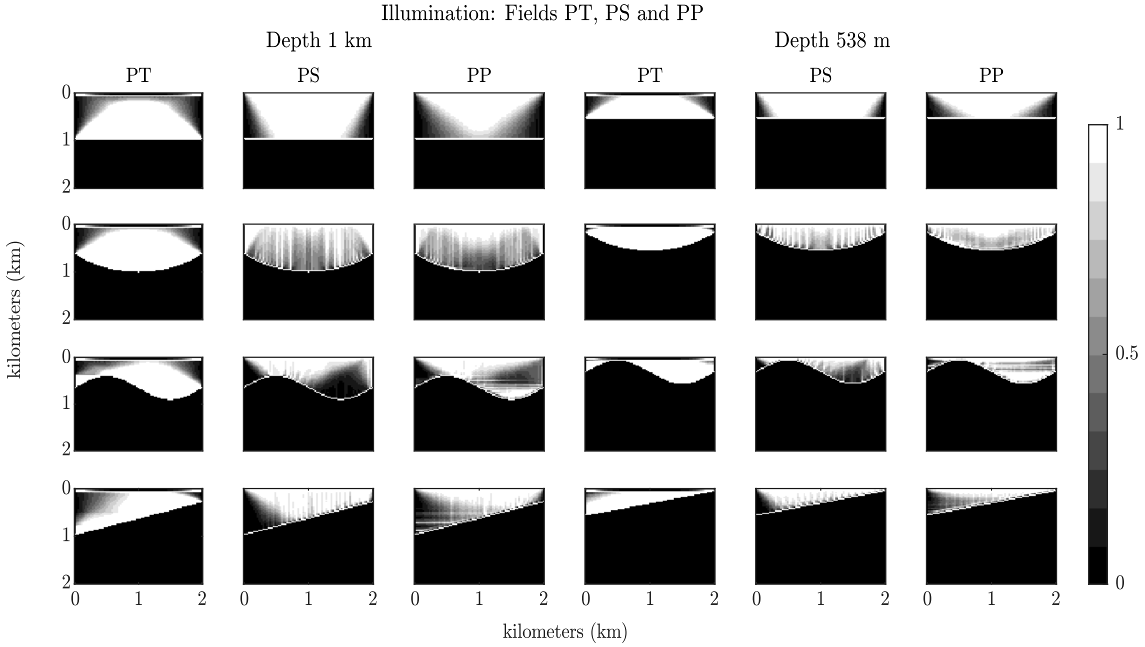

As it was described in the calculation of the adjoints, the fast sweeping algorithm is used to define with a binary variable: 1 for illuminated points, 0 for unilluminated points.

operators that update the velocity models V_s and V_p on Ω_2 can be performed again. This process can be carried out for the different PS-PP arrival time events distinguishable in the shot gather.

8. Conclusion

An innovative inversion algorithm for PS-PP converted wave tomography is introduced. This algorithm is based on an interface model that uses the Level Set function ($\phi(x,z)=0$). PS conversions and PP reflections (direct problem) are simulated in this model, and velocities are jointly inverted with the reflector $[\boldsymbol{\phi}, \boldsymbol{V_s}, \boldsymbol{V_p}]$ ←**Tomo_PS-PP(**$\boldsymbol{\phi^{k=0}}$**,**$\boldsymbol{V_s^{k=0}}$**,**$\boldsymbol{V_p^{k=0}}$**)**. The PS-PP first arrival times are calculated using the FMM in our PS-PP tomography proposal, resulting in a residual with the observed arrival times. The inversion is carried out through an adjoint formulation, developed from variational calculus, to minimize temporal residuals by optimally determining $\phi(x,z)$ (reflector), V_s, and V_p, which are computed using FSM. The formulated multivariate inversion method can be used to estimate one or two variables at a time, treating the others as known, or all three variables (velocities and reflector) simultaneously.

The tests performed show that the convergence of the inversion of $\phi(x,z)$, V_s and V_p is mainly influenced by the illumination irregularity of both PS and PP fields given by the multicomponent seismic acquisition, despite the solution uncertainty depending only on the PS-PP time residual. Consequently, the proposed tomography technique could be improved by increasing the illumination uniformity above Ω_1. The methods established in Hu et al. (2021) and Zhang et al. (2023) could prove beneficial in this respect. On the other hand, the tomography results are closer to the true values when a variable, either V_s or V_p, is known. Better results are obtained if V_p is known, since this information indirectly helps to determine T_{ps}, which is crucial for correctly inverting V_s. Comparable results are obtained when V_p and ϕ are inverted simultaneously, given V_s. However, V_s does not contribute to the calculation of T_{pp}.

This technique is recommended as a first approximation for other methods, such as full waveform inversion to achieve better convergence results, as discussed in Kadu et al. (2016) and Dorn and Wu (2021), or in the case of elastic inversion, as described in Lamert et al. (2018), where the contour $\phi(x, z) = 0$ is used to predict interference regions.

9. Recommendations

Improve the illumination distribution within Ω_1 using algorithms such as the one presented in (Zhang et al., 2023) or in (Hu et al., 2021) so that the velocity model estimates (Vs and Vp) as well as the reflector ($\phi = 0$) are improved with respect to the true ones. Consequently, an improvement in the convergence times of the developed PS-PP tomography algorithm can be achieved.

Given the improvement in illumination uniformity by eliminating discontinuities, better estimates of V_s and V_p can be achieved, which whereon improve the definition of the reflector with the Level Set function ($\phi = 0$). Progress that allows the use of algorithms such as the multiparametric L-BFGS (quasi-Newton), which tunes in each iteration the parameters $\varPsi$, η, and ζ, making the inversion of ϕ, V_s and V_p of better quality and with faster convergence, as indicated in (Bollapragada et al., 2018).

The developed PS-PP tomography methodology can be extended to the following subsurface sublayers. For this purpose, the next to the first arrivals of the PS and PP waves in the gathers, observed travel times of conversions and reflections from the second reflector are selected. The methodology will take the arrival times at the first reflector as sources that transmit energy to the next layer until reaching the next reflector, likewise modeled with $\phi = 0$. It is recommended to use this technique as a first approximation for other methods such as full waveform inversion to operate with better convergence results.

References

Aghasi, A., Kilmer, M., and Miller, E. L. (2011). Parametric level set methods for inverse problems. *SIAM Journal on Imaging Sciences*, 4(2):618–650. pages 2, 11, 14

Álvarez, C. and Coutinho, A. (2013). On computing distance function for level set method using usfem/rothe as stabilized formulation. *Revista Internacional de Métodos Numéricos para Cálculo y Diseño en Ingeniería*, 29(4). pages 26

Arfken, G. B. and Weber, H. J. (1999). Mathematical methods for physicists. pages 14

Bollapragada, R., Nocedal, J., Mudigere, D., Shi, H.-J., and Tang, P. T. P. (2018). A progressive batching l-bfgs method for machine learning. In *International Conference on Machine Learning*, pages 620–629. PMLR. pages 72, 77

Bording, R. P., Gersztenkorn, A., Lines, L. R., Scales, J. A., and Treitel, S. (1987). Applications of seismic travel-time tomography. *Geophysical Journal International*, 90(2):285–303. pages 8, 9, 12, 13

Cameron, M., Fomel, S., and Sethian, J. (2007). Inverse problem in seismic imaging. In *PAMM: Proceedings in Applied Mathematics and Mechanics*, volume 7, pages 1024803–1024804. Wiley Online Library. pages 10

Daniel, K. (2019). 2d parallel first-arrival traveltime modelling and inversion code. pages 41

Demanet, L. (2016). Waves and imaging class notes-18.325. pages 11

Dorn, O. and Wu, Y. (2021). Shape reconstruction in seismic full waveform inversion using a level set approach and time reversal. *Journal of Computational Physics*, 427:110059. pages 12, 76

Engl, H. W. and Groetsch, C. W. (2014). *Inverse and ill-posed problems*, volume 4. Elsevier. pages 10

Farfour, M. and Yoon, W. J. (2016). A review on multicomponent seismology: A potential seismic application for reservoir characterization. *Journal of advanced research*, 7(3):515–524. pages 2, 3, 8

Fomel, S. (1997). A variation formulation of the fast marching eikonal solver: Sep-95. pages 8

Fomel, S. and Backus, M. M. (2003). Multicomponent seismic data registration by least squares. In *2003 SEG Annual Meeting*. OnePetro. pages 9

Hansen, H. H., Pernot, M., Chatelin, S., Tanter, M., and de Korte, C. L. (2015). Shear wave elastography for lipid content detection in transverse arterial cross-sections. In *2015 IEEE International Ultrasonics Symposium (IUS)*, pages 1–4. IEEE. pages 3

Hardage, B. A., DeAngelo, M. V., Murray, P. E., and Sava, D. (2011). *Multicomponent seismic technology*. Society of Exploration Geophysicists. pages 8

Hassouna, M. S. and Farag, A. A. (2007). Multistencils fast marching methods: A highly accurate solution to the eikonal equation on cartesian domains. *IEEE transactions on pattern analysis and machine intelligence*, 29(9):1563–1574. pages 20, 36, 39

Hilterman, F. J. (2001). *Seismic amplitude interpretation*. Society of Exploration Geophysicists and European Association of . . . . pages 89

Hu, J., Qian, J., Cao, J., Wang, X., Wang, H., and Leung, S. (2021). Ray-illumination compensation for adjoint-state first-arrival traveltime tomography. *Geophysics*, 86(5):U109–U119. pages 70, 75, 77

Huang, J.-W. and Bellefleur, G. (2012). Joint transmission and reflection traveltime tomography using the fast sweeping method and the adjoint-state technique. *Geophysical Journal International*, 188(2):570–582. pages 13

Kabanikhin, S. I. (2008). Definitions and examples of inverse and ill-posed problems. pages 10

Kadu, A., van Leeuwen, T., and Mulder, W. A. (2016). Salt reconstruction in full-waveform inversion with a parametric level-set method. *IEEE Transactions on Computational Imaging*, 3(2):305–315. pages 12, 76

Kroon, D. (2009). Accurate fast marching. *Toolbox, Matlab Central website*, 23. pages 36, 39

Lamert, A., Nguyen, L. T., Friederich, W., and Nestorović, T. (2018). Imaging disturbance zones ahead of a tunnel by elastic full-waveform inversion: Adjoint gradient based inversion vs. parameter space reduction using a level-set method. *Underground Space*, 3(1):21–33. pages 12, 76

Leung, S. and Qian, J. (2006). An adjoint state method for three-dimensional transmission traveltime tomography using first-arrivals. pages 13, 24, 41, 45

Li, C., Xu, C., Gui, C., and Fox, M. D. (2010). Distance regularized level set evolution and its application to image segmentation. *IEEE transactions on image processing*, 19(12):3243–3254. pages 44

Li, W. and Leung, S. (2013). A fast local level set adjoint state method for first arrival transmission traveltime tomography with discontinuous slowness. *Geophysical Journal International*, 195(1):582–596. pages 11, 26, 47, 87

Li, W., Leung, S., and Qian, J. (2014). A level-set adjoint-state method for crosswell transmission-reflection traveltime tomography. *Geophysical Journal International*, 199(1):348–367. pages 4, 12, 13, 14, 23, 34, 38, 45, 68, 73

Li, X.-Y. and Zhang, Y.-G. (2011). Seismic reservoir characterization: how can multicomponent data help? *Journal of Geophysics and Engineering*, 8(2):123–141. pages 8

Liu, D. C. and Nocedal, J. (1989). On the limited memory bfgs method for large scale optimization. *Mathematical programming*, 45(1-3):503–528. pages 72

Mathewson, J., Woodward, M. J., Nichols, D., Xu, C., and Leone, C. (2013). Joint pp/ps tomography with floating event constraints. pages 8, 10

Menke, W. (2012). Describing inverse problems. *Geophysical Data Analysis*, pages 1–15. pages 1

Nelson, G. D. and Vidale, J. E. (1990). Earthquake locations by 3-d finite-difference travel times. *Bulletin of the Seismological Society of America*, 80(2):395–410. pages

Niño, C., Duarte, C., Agudelo, W., Sierra, D., and Sacchi, M. (2022). Converted wave travel time computation using a fast marching method and level set interface location. *GeoConvention 2022*. pages 22

Niño, C., Duarte, C., Agudelo, W., and D.A. Sierra and, M. D. S. (2023). Converted wave tomography based on inverse level set and adjoint formulation. In *Geophysical Journal International*, pages 1–23. SUBMITTED PAPER. pages 10

Osher, S. and Fedkiw, R. P. (2005). *Level set methods and dynamic implicit surfaces*, volume 1. Springer New York. pages 10, 11, 14, 44, 46

Pelissier, F. A. (2023). Cell segmentation and tracking. pages 46

Plessix, R.-E. (2006). A review of the adjoint-state method for computing the gradient of a functional with geophysical applications. *Geophysical Journal International*, 167(2):495–503. pages 7, 24, 28

Prieto, K. and Dorn, O. (2016). Sparsity and level set regularization for diffuse optical tomography using a transport model in 2d. *Inverse Problems*, 33(1):014001. pages 11, 14

Rawlinson, N. and Sambridge, M. (2005). The fast marching method: an effective tool for tomographic imaging and tracking multiple phases in complex layered media. *Exploration Geophysics*, 36(4):341–350. pages 13, 21, 22

Stewart, R. R., Gaiser, J. E., Brown, R. J., and Lawton, D. C. (2002). Converted-wave seismic exploration: Methodsconverted-wave seismic exploration: Methods. *Geophysics*, 67(5):1348–1363. pages 8

Taillandier, C., Noble, M., Chauris, H., and Calandra, H. (2009). First-arrival traveltime tomography based on the adjoint-state method. *Geophysics*, 74(6):WCB1–WCB10. pages 13, 24, 37, 41

Treister, E. and Haber, E. (2016). A fast marching algorithm for the factored eikonal equation. *Journal of Computational physics*, 324:210–225. pages 20

Tsai, Y.-H. R. and Osher, S. (2005). Total variation and level set methods in image science. *Acta Numerica*, 14:509–573. pages 26

Wang, F., Xie, X., Pei, Z., and Dong, L. (2022). Anomalous areas detection in rocks using time-difference adjoint tomography. *Mathematics*, 10(7):1069. pages 44, 68

Wang, M., Wang, G., Zhang, S., and Zhao, J. (2010). Electrical impedance tomography based on tikhonov regularization method improved by level set method. In *2010 3rd International Conference on Biomedical Engineering and Informatics*, volume 1, pages 222–225. IEEE. pages 2, 11

Yilmaz, Ö. (2001). *Seismic data analysis: Processing, inversion, and interpretation of seismic data*. Society of exploration geophysicists. pages 8

Yilmaz, Ö. (2015). *Engineering seismology with applications to geotechnical engineering*. Society of Exploration Geophysicists. pages 12, 13

Zeng, J., Pang, J., Sun, W., and Cheung, G. (2019). Deep graph laplacian regularization for robust denoising of real images. In *Proceedings of the IEEE/CVF Conference on Computer Vision and Pattern Recognition Workshops*, pages 0–0. pages

Zhang, J., Dong, L., Wang, J., and Huang, C. (2023). Preconditioned transmission+ reflection joint traveltime tomography with adjoint-state method for subsurface velocity model building. *Geophysical Prospecting*, 71(2):171–190. pages 71, 75, 77

Zhao, H. (2005). A fast sweeping method for eikonal equations. *Mathematics of computation*, 74(250):603–627. pages 7

Zheglova, P. and Farquharson, C. (2012). Level set method in seismic inversion: 2d reconstruction of boundaries. pages 11, 12, 13, 14, 24, 68

Appendixes

Appendix A. Time, Velocities, and Oobjetive Function Variationals

To simplify the notation, let us define $T_{ps} = T_{ps}(\phi, S_{p1}, S_{s1})$ and $T_{ps}^{+\delta} = T_{ps}(\phi + \epsilon \cdot \nu\widetilde{\phi}, S_{p1} + \epsilon \cdot \widetilde{S}_{p1}, S_{s1} + \epsilon \cdot \widetilde{S}_{s1})$, for PS field. The algebraic procedure for the PP field is similar. The first variational of the objective function, is calculated using the following mathematical development.

The first variational of the objective function is defined as:

$$\frac{\delta E}{\epsilon} = \frac{E^{+\delta} - E}{\epsilon}. \tag{44}$$

Where:

$$E = \frac{1}{2}\int_{\partial\Omega=\Gamma} |T_{ps} - T_{ps}^{obs}|^2 ds \;\; E^{+\boldsymbol{\delta}} = \frac{1}{2}\int_{\partial\Omega=\Gamma} |T_{ps}^{+\boldsymbol{\delta}} - T_{ps}^{obs}|^2 ds \tag{45}$$

Considering the absolute value property $\left|T_{ps}^{+\boldsymbol{\delta}} - T_{ps}^{obs}\right|^2 = \left(T_{ps}^{+\boldsymbol{\delta}} - T_{ps}^{obs}\right)^2$, the quadratic term in (44) can be expended and the first variational is:

$$\frac{\delta E}{\epsilon} = \frac{1}{2\epsilon}\int_{\partial\Omega=\Gamma} (T_{ps}^{+\boldsymbol{\delta}2} - T_{ps}^2 - 2(T_{ps}^{+\boldsymbol{\delta}} - T_{ps})T_{ps}^{obs}) ds, \tag{46}$$

This equation can be simplified by introducing the time variation $(T_{ps}^{+\boldsymbol{\delta}} - T_{ps}) = \epsilon\widetilde{T}_{ps}$ to:

$$\frac{\delta E}{\epsilon} = \int_{\partial\Omega=\Gamma} \widetilde{T}_{ps}(T_{ps} - T_{ps}^{obs}) ds. \tag{47}$$

In order to obtain the variational eikonal equation, the following algebraic operations are performed:

$$|\nabla T_{ps}| = Ss \;\rightarrow\; (\nabla T_{ps}^{2}) = (S_{s}^{2}), \tag{48}$$

thus $\nabla T_{ps}^{+\boldsymbol{\delta}2} = S_{s}^{+\boldsymbol{\delta}2}$, how by using ($T_{ps}^{+\boldsymbol{\delta}} = T_{ps} + \epsilon\widetilde{T}_{ps}$):

$$\nabla(T_{ps} + \epsilon\widetilde{T}_{ps}) = S_{s}^{+\boldsymbol{\delta}2} \tag{49}$$

Thus, leading to the Equation (9).

Now, in order to compute the velocity variational, the assignment of P and S field velocities to Ω_1 and Ω_2 spatial regions using the Heaviside function determined by the ϕ geometry function. The discontinuity is smoothed by the tangent function fitted with the factor τ:

$$H_{\tau}(\phi) = \frac{1}{2}(tanh(\frac{\phi}{\tau}) + 1). \tag{50}$$

Consequently, the slowness (for the field S) is defined mathematically using the heaviside function as in:

$$S_{s} = S_{s1}(1 - H_{\tau}(\phi)) + S_{s2}H_{\tau}\phi \tag{51}$$

Thus, a slowness variational ($\delta S = Ss^{\boldsymbol{\delta}} - Ss$) can be determined as:

$$\begin{aligned} \delta S = (S_{s2} - S_{s1}) \cdot (H_{\tau}(\phi + \epsilon\widetilde{\phi}) - H_{\tau}(\phi)) \\ + \epsilon\widetilde{S}s1 \cdot (1 - H_{\tau}(\phi + \epsilon\widetilde{\phi})) + \epsilon\widetilde{S}s2 \cdot H_{\tau}(\phi + \epsilon\widetilde{\phi}) \end{aligned} \tag{52}$$

Figure 16

Determinations of the internal field inside a closed surface from boundary measurements: Green's Theorem

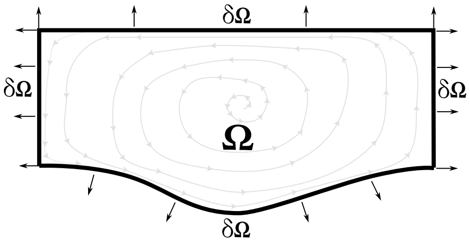

Where:

$$H_\tau(\phi + \epsilon\widetilde{\phi}) = H_\tau(\phi) + \epsilon\widetilde{\phi} \cdot \frac{1}{2\tau \cdot cosh\frac{\phi}{\tau}}. \tag{53}$$

These equations are also used in Li and Leung (2013).

Appendix B. Green's theorem

For the design of the adjoint state, the green theorem must be considered.

Green's First Identity:

$$\boxed{\oint_{\delta\Omega} f(\frac{\partial g}{\partial n})ds = \int_\Omega (\nabla f \cdot \nabla g + f \cdot (div(\nabla g))d\Omega}$$

Another important relationship is the divergence theorem:

$$\boxed{\int_\Omega (div(f))d\Omega = \oint_{\delta\Omega} f \cdot nds}$$

Green's identities help to eliminate the dependence on the variational gradients of times $\widetilde{T}_{pp}$ and $\widetilde{T}_{ps}$.From Equations (19), the first variational of the objetive function is:

$$\begin{aligned}\frac{\delta E}{\epsilon} &= \int_{\Gamma}(\widetilde{T}_{ps}(T_{ps}-T_{ps}^{obs}))ds + \int_{\Gamma}(\widetilde{T}_{pp}(T_{pp}-T_{pp}^{obs}))ds \\ &+ \int_{\Omega_1}(\lambda w_{ps})ds - \underbrace{\int_{\Omega_1}(\lambda\nabla\widetilde{T}_{ps}(\nabla T_{ps}(\phi,S_p,S_s)))d\Omega_1}_{Green} \\ &+ \int_{\Omega_1}(\mu w_{pp})ds - \underbrace{\int_{\Omega_1}\mu\nabla\widetilde{T}_{pp}(\nabla T_{pp}(\phi,S_p))d\Omega_1}_{Green} + \mathcal{O}(\epsilon^2)\ .\end{aligned} \tag{54}$$

The adjoint operators are designed such that on Γ part 1 eliminates part 4, and part 2 eliminates part 6. Finally, parts 3 and 5 are eliminated from the first variational of the objective function, in order to avoid computing $\widetilde{T}_{pp}$ and $\widetilde{T}_{ps}$, by designing adjoint operators that when multiplied by gradients (∇T_{pp} and ∇T_{ps}) hare a divergence equals to zero.

$$\begin{aligned}\frac{\delta E}{\epsilon} &= \overbrace{\int_{\Gamma}(\widetilde{T}_{ps}(T_{ps}-T_{ps}^{obs}))ds}^{part\ 1} + \overbrace{\int_{\Gamma}(\widetilde{T}_{pp}(T_{pp}-T_{pp}^{obs}))ds}^{part\ 2} \\ &+ \int_{\Omega_1}\lambda w_{ps}\ ds + \underbrace{\overbrace{\int_{\Omega_1} div(\lambda\nabla T_{ps}(\phi,S_p,S_s))\widetilde{T}_{ps}\ d\Omega_1}^{part\ 3} - \overbrace{\int_{\delta\Omega_1}\lambda\frac{\partial T_{ps}(\phi,S_p,S_s)}{\partial n}\widetilde{T}_{ps}\ ds}^{part\ 4}}_{Green} \\ &+ \int_{\Omega_1}\mu w_{pp}\ ds + \underbrace{\overbrace{\int_{\Omega_1} div(\mu\nabla T_{pp}(\phi,S_p))\widetilde{T}_{pp}\ d\Omega_1}^{part\ 5} - \overbrace{\int_{\delta\Omega_1}\mu\frac{\partial T_{pp}(\phi,Sp)}{\partial n}\widetilde{T}_{pp}\ ds}^{part\ 6}}_{Green} \\ &+ \mathcal{O}(\epsilon^2)\ .\end{aligned} \tag{55}$$

In equation (55), the adjoint operators are designed such that on Γ part 1 eliminates part 4 of the equation, and part 2 eliminates part 6. The adjoints must also eliminate parts

3 and 5 of equation (55).

Appendix C. Adjoints $\hat{\lambda}$ and $\hat{\mu}$ on the Reflector

The processing of reflection seismic data provides an image of the geological subsurface. The geometry of the path of the incident P (compressional) wave, generated by the source S1 in Figure 17, encounters a change in the elastic properties of materials at an interface where part of the energy is reflected with a P-to-P reflection angle equal to the angle of incidence and recorded at the receiver R2. The angle of reflection for the converted P-to-S wave is less than the angle of incidence and follows an asymmetric trajectory recorded at receiver position R1. The remaining energy is transmitted to the other medium (refracted waves) with changes in propagation direction, speed and mode.

The propagation of the computed adjoint for the fields PS-PP, λ and μ interacts with the reflector $\phi(x, z) = 0$. This interaction ensures that the variational components of the travel times, represented by the transmission times Tpt, remain preserved at this boundary, as mentioned in Hilterman (2001). Using the physical constraint imposed by the eikonal equation for the propagation times T_{pt}, the equations in (56) are constructed.

$$\begin{aligned}\frac{\delta E}{\epsilon} &= \int_{\Omega_1} (\lambda w_{ps})\ ds + \int_{\Omega_1} (\mu w_{pp})\ ds - \int_R \lambda \frac{\partial T_{ps}(\phi, S_p, S_s)}{\partial n} \widetilde{T}_{pt} ds - \int_R \mu \frac{\partial T_{pp}(\phi, S_p)}{\partial n} \widetilde{T}_{pt}\ ds \\ &+ \int_{\Omega_1} \hat{\lambda}(w_{pt} - \nabla \widetilde{T}_{pt}(\nabla T_{pt}(\phi, S_p))) d\Omega_1 + \int_{\Omega_1} \hat{\mu}(w_{pt} - \nabla \widetilde{T}_{pt}(\nabla T_{pt}(\phi, S_p))) d\Omega_1 + \mathcal{O}(\epsilon^2)\ . \end{aligned} \tag{56}$$

The equation (56) requires the use of Green's first identity to suppress the variational

Figure 17

Seismic reflection plane waves at oblique angle mode conversion related to time gradient direction with the normal to the surface.

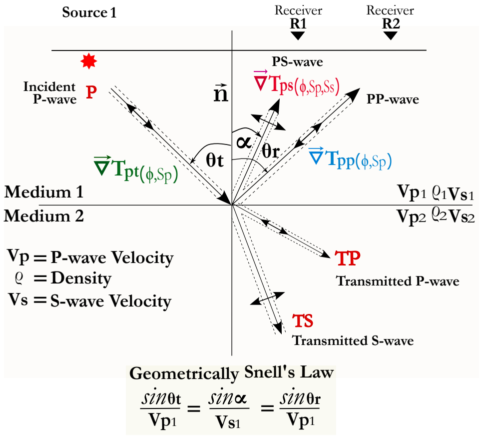

components of the remaining times.

$$
\begin{aligned}
\frac{\delta E}{\epsilon} = & \int_{\Omega_1} \lambda w_{ps} ds + \int_{\Omega_1} \mu w_{pp} ds + \int_{\Omega_1} \hat{\mu} w_{pt} dx + \int_{\Omega_1} \hat{\lambda} w_{pt} dx \\
& - \underbrace{\int_R \lambda \frac{\partial T_{ps}(\phi, S_p, S_s)}{\partial n} \widetilde{T}_{pt} \ ds}_{part \ 1} - \underbrace{\int_R \mu \frac{\partial T_{pp}(\phi, S_p)}{\partial n} \widetilde{T}_{pt} \ ds}_{part \ 2} \\
& + \int_{\Omega_1} div(\hat{\lambda} \nabla T_{pt}(\phi, S_p, S_s)) \nabla \widetilde{T}_{pt} d\Omega_1 - \underbrace{\int_{\delta\Omega_1} \hat{\lambda} \frac{\partial T_{pt}(\phi, S_p)}{\partial n} \widetilde{T}_{pt} \ ds}_{part \ 3} \qquad (57) \\
& + \int_{\Omega_1} div(\hat{\mu} \nabla T_{pt}(\phi, S_p, S_s)) \nabla \widetilde{T}_{pt} \ d\Omega_1 - \underbrace{\int_{\delta\Omega_1} \hat{\mu} \frac{\partial T_{pt}(\phi, S_p)}{\partial n} \widetilde{T}_{pt} \ ds}_{part \ 4} + \mathcal{O}(\epsilon^2)
\end{aligned}
$$

These geometric identities enable the construction of the adjoint $\hat{\lambda}$ and $\hat{\mu}$. By starting with the equations of the adjoint with initial conditions away from the reflector, the equation

(57) can be simplified into (35):

$$\frac{\delta E}{\epsilon} = \int_{\Omega_1} \lambda w_{ps} \; d\Omega_1 + \int_{\Omega_1} \mu w_{pp} \; d\Omega_1 + \int_{\Omega_1} \hat{\mu} w_{pt} \; d\Omega_1 + \int_{\Omega_1} \hat{\lambda} w_{pt} \; d\Omega_1 + \mathcal{O}(\epsilon^2) \tag{58}$$

In the equation (57) it is proposed that part 1 can be eliminated with part 3, just as part 4 eliminates part 2, by applying geometric relations of the behaviour of the time gradients ∇T_{pt}, ∇T_{pp} and ∇T_{ps} with the normal vector ($\vec{n}$) at an interface point, as shown in figure 17. The solution of the equation is completed by knowing that for the P-field $w_{pt} = w_{pp}$ in Ω_1, which allows obtaining an expression for the solution of the perturbations that optimally update the variables: ϕ, S_p and S_s.

Appendix D. Glossary

Term	**Definition**
$\phi(x,z)=0$	Zero contour of the Level Set function, represents the true reflector (R)
ϕ, S_{s1}, S_{p1}	Parametros a invertir: Modelo reflector, lentitud P y S
$\widetilde{\phi}, \widetilde{S}_{s1}, \widetilde{S}_{p1}$	Perturbacion de actualizacion
Ω_1	Region defined by $\phi(x,z) \leq 0$
$\delta\Omega_1$	The boundary of the region Ω_1
$T_{ps}(\phi, S_{p1}, S_{s1})$	The travel time from the reflector (where $\phi(x,z)=0$) to the surface (Γ) is determined by the velocity V_s in the medium Ω_1.
$T_{ps}^{obs,i}$	Travel time of the converted PS wave recorded by a multicomponent geophone on the surface.
$\widetilde{T}_{ps}$	time variational
$T_{pt}(\phi, S_{p1})$	Tiempo de viaje onda P transmitida de fuente a el reflector $\phi=0$ dada una lentitud del medio Sp.
$\theta_t, \alpha, \theta_r$	Arrival, conversion, and reflection angles on the reflector modeled with $\phi(x,z)=0$ are being referred to.
w_{ps}, w_{ps}	variacional de lentitude del campo PS and PP
$\frac{\partial T_{pt}(\phi,S_p)}{\partial n}$	Derivada direccional sobre la normal a la superficie
λ,μ	Adjoint fields originated from the residuals of PS-PP wave travel times given on the free surface Γ.
$\hat{\lambda}$,$\hat{\mu}$	Adjoint fields of PS and PP waves originating from the reflector where $\phi=0$.
R.errTps, R.errTpp	Errors between modelled and observed travel times, for PS and PP fields
APE	The absolute percentage error
MAPE	Calculation of the mean absolute difference between the location of the true reflector (Pts_R) with the modeled one, ϕ_0